UNIVERSIDAD DE CONCEPCIÓN
FACULTAD DE CIENCIAS FÍSICAS Y MATEMÁTICAS

REMOLINOS EN EL GOLFO DE ANCUD: UN ANÁLISIS NUMÉRICO

Por: Tomás Elías Valderrama Platz

Tesis presentada a la Facultad de Ciencias Físicas y Matemáticas de la Universidad de Concepción para optar al título profesional de Geofísico

Agosto 2025
Concepción, Chile

Profesor Guía: Dr. Héctor Hito Andrés Sepúlveda Allende
Comisión: Dr. Osvaldo Artal, Dra. Carolina Parada, Dr. Oscar Pizarro

REMOLINOS EN EL GOLFO DE ANCUD: UN ANÁLISIS NUMÉRICO

Por: Tomás Elías Valderrama Platz

Tesis presentada a la Facultad de Ciencias Físicas y Matemáticas de la Universidad de Concepción para optar al título profesional de Geofísico

Agosto 2025
Concepción, Chile

DGEO, 2025

Profesor Guía: Dr. Héctor Hito Andrés Sepúlveda Allende
Comisión: Dr. Osvaldo Artal, Dra. Carolina Parada, Dr. Oscar Pizarro

Agradecimientos

Este trabajo fue financiado por el proyecto FONDECYT Regular N°1211230, *"Modelling the role of biogeochemical river input into fjord systems in Chilean Patagonia."*

Las simulaciones se realizaron utilizando recursos computacionales del Laboratorio Nacional de Computación de Alto Rendimiento (NLHPC), Chile.

Índice general

Índice de tablas

Índice de figuras

Resumen

Esta investigación analiza el origen y la dinámica de remolinos de mesoescala en el Golfo de Ancud (41,8°–42,2°S, 73,5°–73,9°O), ubicado en el Mar Interior de Chiloé (MIC), Chile. Se realizaron simulaciones numéricas de alta resolución con el modelo CROCO, complementadas con experimentos de sensibilidad y descomposición armónica de mareas, para evaluar la influencia de distintos forzamientos—incluyendo mareas astronómicas, batimetría local y vientos climatológicos—en la formación y evolución de los remolinos. Los experimentos de sensibilidad incluyeron: (i) eliminación de la componente mareal, (ii) un escenario con batimetría plana a 150 m de profundidad, y (iii) simulaciones forzadas únicamente por vientos climatológicos. Cada experimento cubrió un mes completo en enero y julio, representando las condiciones de verano e invierno.

Los resultados muestran que los remolinos de mesoescala son estructuras persistentes y dominantes en el Golfo de Ancud, con diámetros típicos de 15–30 km, duraciones de varias semanas y marcada variabilidad estacional. En verano, los remolinos presentan mayor intensidad y concentración, alcanzando velocidades superficiales máximas de hasta 20 cm/s, mientras que en invierno se distribuyen de manera más dispersa y con menor intensidad, aunque mantienen coherencia en profundidad. Los experimentos sin mareas confirman que las mareas astronómicas no son determinantes en la generación de los remolinos, aunque sí pueden modular su intensidad y estabilidad. La batimetría y la circulación regional son los principales factores que controlan su ubicación y estructura.

Estos hallazgos indican que los remolinos de mesoescala son elementos intrínsecos de la circulación local en el Golfo de Ancud, y no estructuras transitorias ni exclusivamente mareales. Este estudio aporta nuevos conocimientos sobre la complejidad dinámica del Mar Interior de Chiloé, resaltando la importancia de considerar el transporte y mezclas inducidos por remolinos en estudios ecológicos, biogeoquímicos y de dispersión de contaminantes. Trabajos futuros podrían incluir análisis de vorticidad y balances de energía, evaluación de variabilidad estacional e interanual, e integración con modelos acoplados océano-atmósfera, permitiendo un entendimiento más profundo de los mecanismos de formación de remolinos, su retroalimentación sobre la circulación regional y sus implicancias para la gestión sostenible del ecosistema marino del sur de Chile.

Abstract

This study investigates the origin and dynamics of mesoscale eddies in the Gulf of Ancud (41.8°–42.2°S, 73.5°–73.9°W), located within the Chiloé Inland Sea (CIS), southern Chile. High-resolution numerical simulations were conducted using the CROCO model, complemented by sensitivity experiments and tidal harmonic decomposition, to assess the influence of different forcings—including astronomical tides, local bathymetry, and climatological winds—on eddy formation and evolution. The sensitivity experiments included: (i) removal of astronomical tides, (ii) a flattened bathymetry scenario (150 m depth), and (iii) simulations forced only by climatological winds. Each experiment covered a full month in January and July to represent summer and winter conditions.

The results demonstrate that mesoscale eddies are persistent and dominant features of the Gulf of Ancud, with typical diameters of 15–30 km, lifetimes of several weeks, and clear seasonal variability. In summer, eddies were stronger and more concentrated, with maximum surface velocities reaching up to 20 cm/s, while in winter they appeared more dispersed and weaker but remained coherent at depth. Experiments removing tidal forcing confirmed that astronomical tides do not play a primary role in eddy generation, although they may modulate intensity and stability. Bathymetry and regional circulation patterns were found to be the main factors controlling the location and structure of these eddies.

These findings indicate that mesoscale eddies are intrinsic elements of the local circulation in the Gulf of Ancud, rather than transient or purely tide-driven features. The study provides new insights into the complexity of the Chiloé Inland Sea dynamics, highlighting the need to consider eddy-induced transport and mixing in ecological, biogeochemical, and pollutant dispersion studies. Future work could include vorticity and energy budget analyses, seasonal and interannual variability assessments, and the integration of coupled ocean-atmosphere models. These approaches would allow for a deeper understanding of eddy formation mechanisms, their feedback on regional circulation, and their implications for sustainable management of the marine ecosystem in southern Chile.

Capítulo 1

Introducción

El Mar Interior de Chiloé (MIC; 41.5°–43.9°S, 72.5°–74.0°W) (Fig. 1.1), ubicado en el sur de Chile, constituye uno de los sistemas estuarinos más extensos del mundo y posee una alta relevancia ecológica y socioeconómica, dado su rol en la provisión de servicios ecosistémicos y su vinculación con actividades productivas como la pesca y la acuicultura (Iriarte et al., 2010). Este sistema está delimitado por la isla de Chiloé al oeste y el continente al este, y se caracteriza por una compleja interacción entre factores geomorfológicos, mareales y atmosféricos. En su interior se desarrollan dos grandes golfos —Ancud (41.7°–42.5°S, 73.0°–74.0°W) (Fig. 1.2) y Corcovado—, además del Seno de Reloncaví y numerosos fiordos y canales, conformando una red hidrográfica de gran complejidad y dinamismo (Gajardo Cortés and Ther Ríos, 2011; Rebolledo, 2012).

La topografía afecta la dirección local del viento en el mar interior de Chiloé (Cáceres et al., 2003; Letelier et al., 2011; Soto-Mardones et al., 2009). En las zonas externas del MIC, la circulación atmosférica regional es el principal factor que determina el viento (Chaigneau and Pizarro, 2005; Letelier, 2010). En Faro Corona, la orientación del canal de Chacao genera direcciones de viento secundarias (Letelier et al., 2011), mientras que las montañas de Chiloé, con alturas superiores a 100 metros, interrumpen la influencia directa del Pacífico sobre el sector oriental del golfo Corcovado (Garreaud and Muñoz, 2005). La intensidad del viento en el golfo de Ancud varía estacionalmente, siendo más fuerte en invierno (6–12 m/s) y moderada en verano (4–8 m/s); mientras que otoño y primavera son estaciones que presentan direcciones variables, con predominio de transiciones entre los patrones de verano e invierno, y una intensidad promedio entre 3 y 8 m/s. Además, el viento presenta una variabilidad adicional según la topografía local y eventos climáticos específicos. Este patrón tiene un impacto directo en la circulación y mezcla de las aguas superficiales, influyendo en los ecosistemas marinos locales (Letelier et al., 2011; Soto-Mardones et al., 2009).

En cuanto a las corrientes, en el canal de Chacao se registran velocidades típicas de hasta 4 m/s (Cáceres et al., 2003). Durante enero de 2016, las velocidades superaron los 2 m/s, con máximos de 6 m/s el 70 % de los días (Artal et al., 2019). En general, se registraron corrientes superiores a 2 m/s entre el 20 y el 30 % de los días, siendo 4 m/s el máximo observado en el canal (Artal et al., 2019). En verano, la circulación superficial presenta patrones consistentes y estables debido a la fuerte estratificación de la columna de agua. La capa superficial, más

Figura 1.1: Ubicación del área de estudio. El recuadro en el mapa de Sudamérica indica el Mar Interior de Chiloé (MIC).

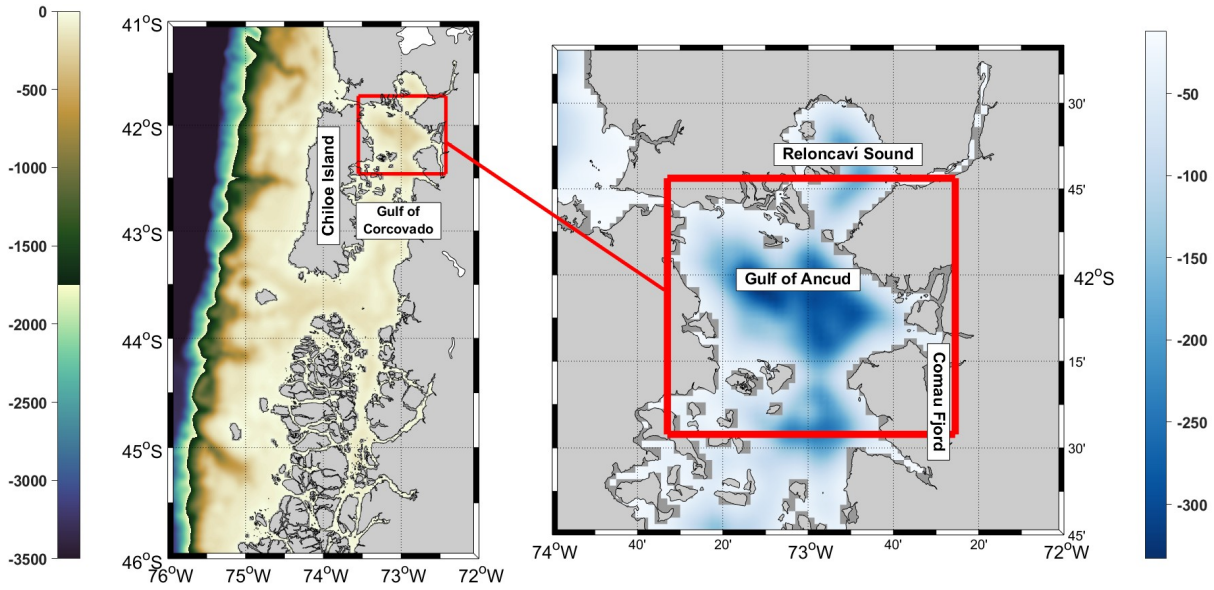

Figura 1.2: Batimetría del modelo MOSA en la Patagonia Norte (izquierda) y zoom del Golfo de Ancud, área de estudio (derecha).

somera y menos densa, se encuentra separada de las masas de agua más profundas, y las mareas y los vientos locales actúan de manera más uniforme sobre esta capa (Letelier et al., 2011; Soto-Mardones et al., 2009). En invierno, en cambio, la mezcla vertical es más intensa debido a la menor estratificación y a la acción de vientos variables. Esto genera turbulencia superficial, lo que explica la ausencia de un patrón claro en los primeros metros. Más en profundidad, las corrientes se estabilizan, ya que las fuerzas de mezcla disminuyen con la profundidad (Letelier et al., 2011; Martínez et al., 2015).

La circulación en el MIC ha sido descrita como un sistema estuarino de dos o tres capas, con un flujo superficial de Agua Estuarina (AE) y capas subyacentes dominadas por Agua Subantártica Modificada (ASAAM) y, en menor medida, Agua Ecuatorial Subsuperficial (AESS) (Sievers et al., 2002a; Silva et al., 1995; Sievers and Silva, 2006). Factores como la topografía submarina, la forzante mareal y el viento regional modulan la dinámica local (Cáceres et al., 2003; Letelier et al., 2011). No obstante, a pesar de la extensa caracterización de la estructura vertical del sistema, aún no se han documentado procesos mesoestructurales como remolinos dentro del MIC, los cuales podrían influir en el intercambio de masas de agua y modificar el patrón de circulación tradicionalmente descrito, especialmente en el golfo de Ancud.

En este contexto, Allel (2020) reportó patrones de circulación cerrada en la superficie del golfo de Ancud, identificados mediante simulaciones de deriva de partículas lagrangianas forzadas con salidas del modelo MOSA, basado en el código CROCO. Dichos experimentos permitieron describir trayectorias de material flotante en la zona, sugiriendo la existencia de

estructuras de recirculación superficial. Sin embargo, aún se desconoce si estas corresponden a remolinos persistentes con extensión vertical significativa, así como los mecanismos físicos responsables de su formación y mantenimiento.

Considerando esta brecha de conocimiento, el presente trabajo tiene como objetivo general identificar el origen y la dinámica del remolino en el Golfo de Ancud. Para ello, se emplearon simulaciones numéricas de alta resolución con el modelo CROCO, complementadas con experimentos de sensibilidad para evaluar la influencia de distintas forzantes, como marea, viento y topografía.

Finalmente, la motivación de este estudio radica en que los remolinos pueden influir significativamente en la circulación local, la dispersión de contaminantes y el transporte de nutrientes, con implicancias directas para la gestión ambiental y la planificación de actividades productivas en el MIC (Vázquez Pinillos et al., 2023).

El documento se organiza de la siguiente manera: el Capítulo 1 corresponde a la Introducción, redactada en español, donde se presentan el propósito de la tesis, los objetivos generales y específicos, así como la hipótesis principal y la hipótesis alternativa. El Capítulo 2 contiene el manuscrito original, redactado en inglés, e incluye las secciones Abstract, Introduction, Methods, Results, Discussion y Conclusions, así como las referencias bibliográficas correspondientes.

1.1. Propósito de la tesis

Objetivo General

Identificar el origen y caracterizar la dinámica de los remolinos en el Golfo de Ancud, evaluando la influencia de factores como la marea, el viento y la topografía mediante simulaciones numéricas de alta resolución.

Objetivos Específicos

1. Describir la circulación superficial y subsuperficial en el Golfo de Ancud utilizando simulaciones numéricas.

2. Identificar y caracterizar los remolinos recurrentes, evaluando su extensión espacial y temporal.

3. Analizar la influencia de la marea, el viento y la topografía en la formación y mantenimiento de los remolinos.

4. Validar los resultados mediante comparación con observaciones disponibles y estudios previos.

Hipótesis

Los remolinos observados en la superficie del Golfo de Ancud son estructuras recurrentes con extensión vertical significativa, cuyo origen y mantenimiento dependen de la interacción entre la marea, el viento y la topografía local.

Hipótesis Alternativa

Los remolinos observados en la superficie del Golfo de Ancud no son estructuras recurrentes ni tienen extensión vertical significativa, y su formación se debe a procesos estocásticos o a otras variables no consideradas en el modelo.

Capítulo 2

Manuscrito

2.1. abstract

This research studies the origin and dynamics of mesoscale eddies in the Gulf of Ancud, located in the Chilean Inland Sea (CIS). Using high-resolution numerical simulations performed with the CROCO model and by means of sensitivity experiments, we sought to identify the forcings responsible for the generation of these eddies in the Gulf. The presence of mesoscale eddies was found to be dominant in the area, and their size, duration and seasonal variability were analyzed. Both harmonic tidal decomposition and simulations without tidal influence revealed that tidal force does not play a crucial role in the generation of these eddies. These eddies are robust elements of the local dynamics, and their formation and maintenance cannot be attributed to specific forcings.

2.2. Introduction

This study focuses on the Chiloé Inland Sea (CIS) (Fig. 2.1), a vast expanse of water located in southern Chile. This body of water is part of the southern fjord belt (Fig. 2.2) and constitutes one of the most extensive estuarine systems in the world, renowned for its ecological and socioeconomic importance (Iriarte et al., 2010).

Figura 2.1: Location of the study area. The inset on the map of South America indicates the Chiloé Inner Sea (CIS).

Estuaries, defined as semi-enclosed coastal water bodies, serve as transition zones between rivers and the ocean. They are characterized by complex circulation patterns and salinity gradients determined by factors such as freshwater input and ocean currents (Shen et al., 2022). Among estuaries, fjords stand out because of their unique geomorphology, shaped by glacial advance and retreat during glacial periods. These formations exhibit highly stratified density structures influenced both by the topography of the sea floor and the properties of the inflowing waters (Andrews et al., 1988). The dynamics of fjords include a longitudinal pressure gradient that generates a two-layer circulation pattern: an upper layer that transports fresh water toward the ocean and a lower layer that brings salt water toward the

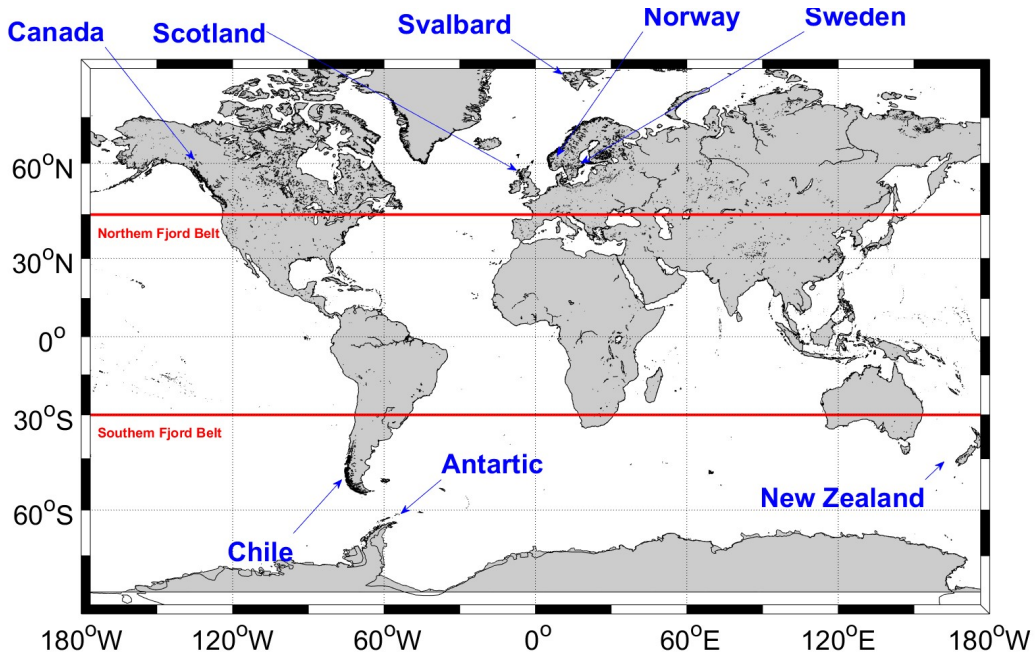

Figura 2.2: Location of the main fjord areas around the world, modified from Howe et al. (2010), who adapted the original figure from Syvitski et al. (1987).

interior. This two-layer circulation is fundamental for the mixing of fresh and salt water, supporting biodiversity and biogeochemical processes in these marine regions (Iriarte et al., 2010).

The CIS is bounded by Chiloé Island to the west and the Chilean mainland to the east, extending approximately between 41.5°S and 43.9°S. This system is highly complex due to the interaction of geomorphology, tidal dynamics, and freshwater inputs. It comprises multiple micro-basins, fjords, and channels, including the Reloncaví Sound, the Gulfs of Ancud and Corcovado, Boca del Guafo, the Moraleda Channel, and the Elefante Estuary (Fig. 2.3). Its underwater relief is intricate, with numerous channels, fjords, bays, and inlets shaped by tidal and current-induced processes. The CIS communicates with the Pacific Ocean mainly through the Chacao Channel in the north, where intense semi-diurnal tidal currents can exceed 4 m s^{-1} during spring tides and about 2 m s^{-1} during neap tides (Artal et al., 2019). These tidal flows play a key role in the exchange of waters between the Pacific Ocean and the inland sea.

The Gulf of Ancud (Fig. 2.3), located within the CIS, is a region of great cultural and economic relevance. The sea underpins the main economic activities of the area, such as artisanal fishing, which remains a cornerstone of local identity and livelihood (Gajardo Cortés and Ther Ríos, 2011). Additionally, seaweed and salmon aquaculture represent highly dynamic industries, although they face environmental and social challenges related to sustainability (Rebolledo, 2012). Together with livestock, agriculture, and tourism, these activities shape a diversified economy that depends closely on the marine environment.

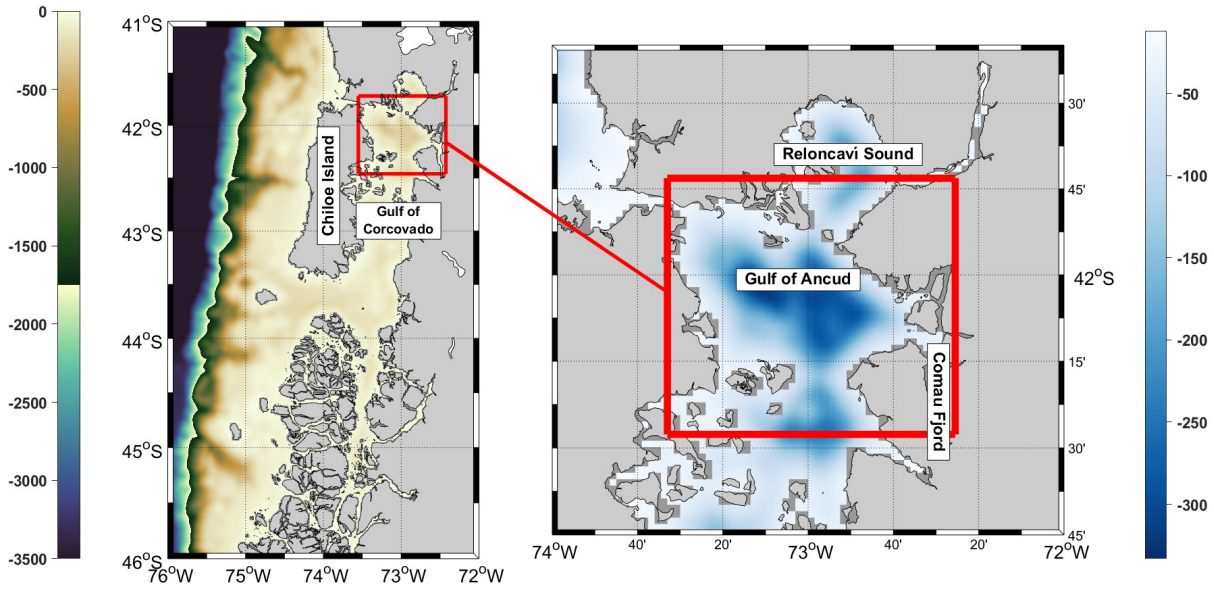

Figura 2.3: Bathymetry from the MOSA model in northern Patagonia (left) and a zoom of the Gulf of Ancud, the study area (right).

This strategic setting highlights the importance of studying the hydrodynamic phenomenon of the eddy observed in the Gulf of Ancud, as it influences marine circulation and the dispersion of pollutants from urban and industrial sources. Understanding the mechanisms and forces driving this eddy is crucial for the effective management of marine ecosystems and the conservation of the coastal environment, providing insights into how industrial and climatic activities affect local dynamics (Vázquez Pinillos et al., 2023).

The circulation of the Chiloé Inland Sea (CIS) has traditionally been described as a two- or three-layer system (Fig. 2.4): a surface layer dominated by fresh water and one or two deeper layers with increasing salinity (Sievers et al., 2002a,b; Sievers and Silva, 2006; Silva et al., 1997, 1995; Strub et al., 2019). Different oceanic water masses converge in this region, particularly the Subantarctic Water (SAW) and the Equatorial Subsurface Water (ESSW), as several studies have documented (Silva et al., 2009; Schneider et al., 2003). These masses interact with freshwater from multiple sources—river discharges, glaciers, coastal runoff, rainfall, and snowmelt—giving rise to new water types, including the Modified Subantarctic Water (MSAW) and the Estuarine Water (EW) (Sievers and Silva, 2006; Pickard, 1971; Silva et al., 1995; Sievers, 2008).

While previous studies have provided valuable descriptions of the vertical structure and general estuarine circulation of the CIS, mesoscale variability—such as the existence of eddies or transient circulation features—has not yet been documented in detail. The present work seeks to address this gap by identifying, for the first time, the existence of an eddy in

the Gulf of Ancud and analyzing the main forcing mechanisms associated with its formation and persistence.

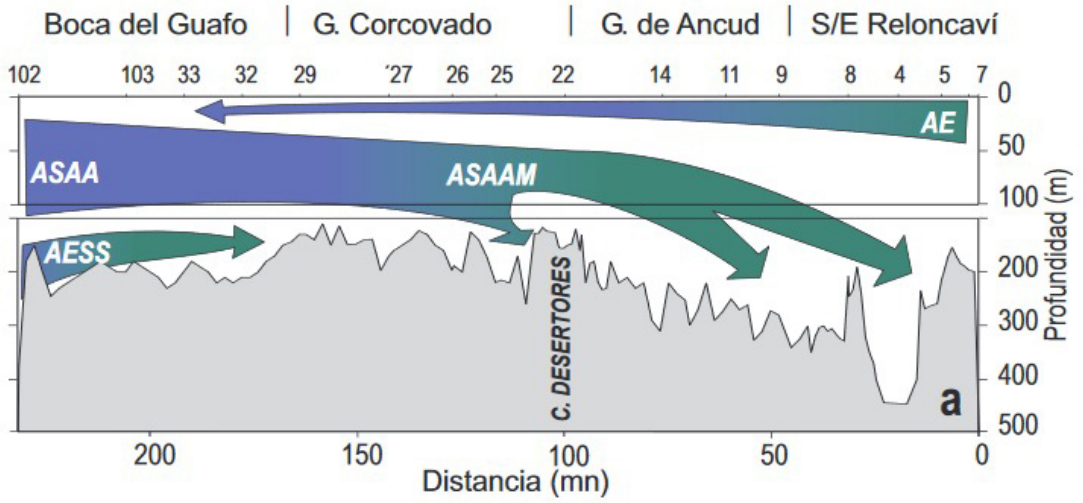

Figura 2.4: Schematic model of the vertical circulation of the Chiloé Inland Sea. Figure taken from Sievers & Silva (2006).

In the upper 50 m, Estuarine Water (EW) predominates, flowing from the Reloncaví Sound toward the Guafo Mouth. Beneath it, down to approximately 100 m depth, lies the Modified Subantarctic Water (MSAW), which forms when Subantarctic Water (SAW) enters through the Guafo Mouth, moves northward, and mixes with EW (Silva et al., 2009; Schneider et al., 2003). This water mass is crucial for quantifying freshwater input to the coasts of western Patagonia (Saldías et al., 2019). The mixture of MSAW and EW dominates in the Gulf of Ancud and extends into the Moraleda Channel, contributing to the ventilation of micro-basins and preventing oxygen depletion (Sievers and Silva, 2006). Conversely, the Equatorial Subsurface Water (ESW) also enters through Boca del Guafo in a northward direction, but its advance is restricted to the southern end of the Corcovado Gulf by regional topographic constraints (Sievers and Silva, 2006). Thus, two layers predominate in the Gulf of Ancud: a shallow layer composed of EW and a deeper layer dominated by MSAW.

The Gulf of Ancud is a semi-enclosed system connected to other basins through channels and passages, and to the Pacific Ocean through the Chacao Channel (Cáceres et al., 2003; Pantoja et al., 2011). Its bathymetry is irregular, reaching depths of up to 300 m (Rodrigo, 2006). The topography limits the entry of water masses and shapes their dynamics, with key features including the Nao (70 m) and Queullín (300 m) passages, which separate it from the Reloncaví Sound (Araya-Vergara et al., 2008); the Chacao Channel (60 m), which connects it to the Pacific Ocean; and the Apiao (120 m) and Desertores (140 m) passages, which separate it from the Corcovado Gulf (González-Carrasco and Díaz-Naveaz, 2012; Silva et al., 1995).

The thermocline in the Gulf of Ancud is located at around 20 m depth, accompanied by weak haloclines and pycnoclines at similar levels. Below 30 m, temperature remains uniform

at approximately 11°C. Salinity is also homogeneous below 20 m, and the distributions of salinity and dissolved oxygen are comparable. Oxygen levels in the Gulf of Ancud and Reloncaví Sound exceed 7 ml L^{-1}, with saturation above 120 %, whereas in the Corcovado Gulf they barely reach 5 ml L^{-1}, corresponding to about 80 % saturation (Silva et al., 1995).

Topography affects local wind direction in the Chiloé inland sea (Cáceres et al., 2003; Letelier et al., 2011; Soto-Mardones et al., 2009). In external areas of the CIS, the regional atmospheric circulation is the main factor determining the wind (Chaigneau and Pizarro, 2005; Letelier, 2010). At Faro Corona, the orientation of the Chacao Channel generates secondary wind directions (Letelier et al., 2011), while the mountains of Chiloé, with heights of over 100 meters, interrupt the direct influence of the Pacific over the eastern sector of the Corcovado Gulf (Garreaud and Muñoz, 2005). The intensity of the wind in the Gulf of Ancud varies seasonally, being stronger in winter (6-12 m/s) and moderate in summer (4-8 m/s); while autumn and spring are seasons that present variable directions, with a predominance of transitions between summer and winter patterns, with an average intensity of between 3 and 8 m/s. In addition, the wind presents additional variability according to local topography and specific climatic events. This pattern has a direct impact on surface water circulation and mixing, influencing local marine ecosystems (Letelier et al., 2011; Soto-Mardones et al., 2009).

Regarding currents, in the Chacao Channel, typical velocities of up to 4m/s are recorded (Cáceres et al., 2003). During January 2016, speeds exceeded 2m/s, with maximums of 6 m/s, 70 % of the days (Artal et al., 2019). In general, currents higher than 2m/s were recorded between 20 and 30 % of the days, with 4m/s being the maximum observed in the channel (Artal et al., 2019). In summer, the surface circulation presents consistent and stable patterns due to the strong stratification of the water column. The shallow, less dense surface layer is separated from the deeper water masses, and local tide and winds act more uniformly in this layer (Letelier et al., 2011; Soto-Mardones et al., 2009). While in winter, vertical mixing is more intense due to less stratification and the action of variable winds. This generates surface turbulence, which explains the lack of a clear pattern in the first few meters. Further down, the currents stabilize, as the mixing forces become less intense with depth (Letelier et al., 2011; Martínez et al., 2015).

Although general patterns of circulation have been described, the dynamics responsible for mesoscale variability in the CIS remain unclear. Recent Lagrangian modeling efforts have provided preliminary evidence of surface circulation patterns in the Gulf of Ancud. Using the OpenDrift code package (Dagestad et al., 2018), Allel (2020) simulated the dispersion of Marine Anthropogenic Debris (MAD) throughout the Los Lagos Region (southern Chile). His simulations revealed circular surface circulation patterns in the Gulf of Ancud during several months of the year—particularly in January, March, April, and December—suggesting the possible presence of an eddy-like structure (Figure 2.5). However, that study was limited to surface-level trajectories, leaving open the question of whether these circular patterns represent a purely superficial phenomenon or a three-dimensional, recurrent hydrodynamic structure. Addressing this uncertainty is essential for understanding the mechanisms that drive circulation and material transport in the region.

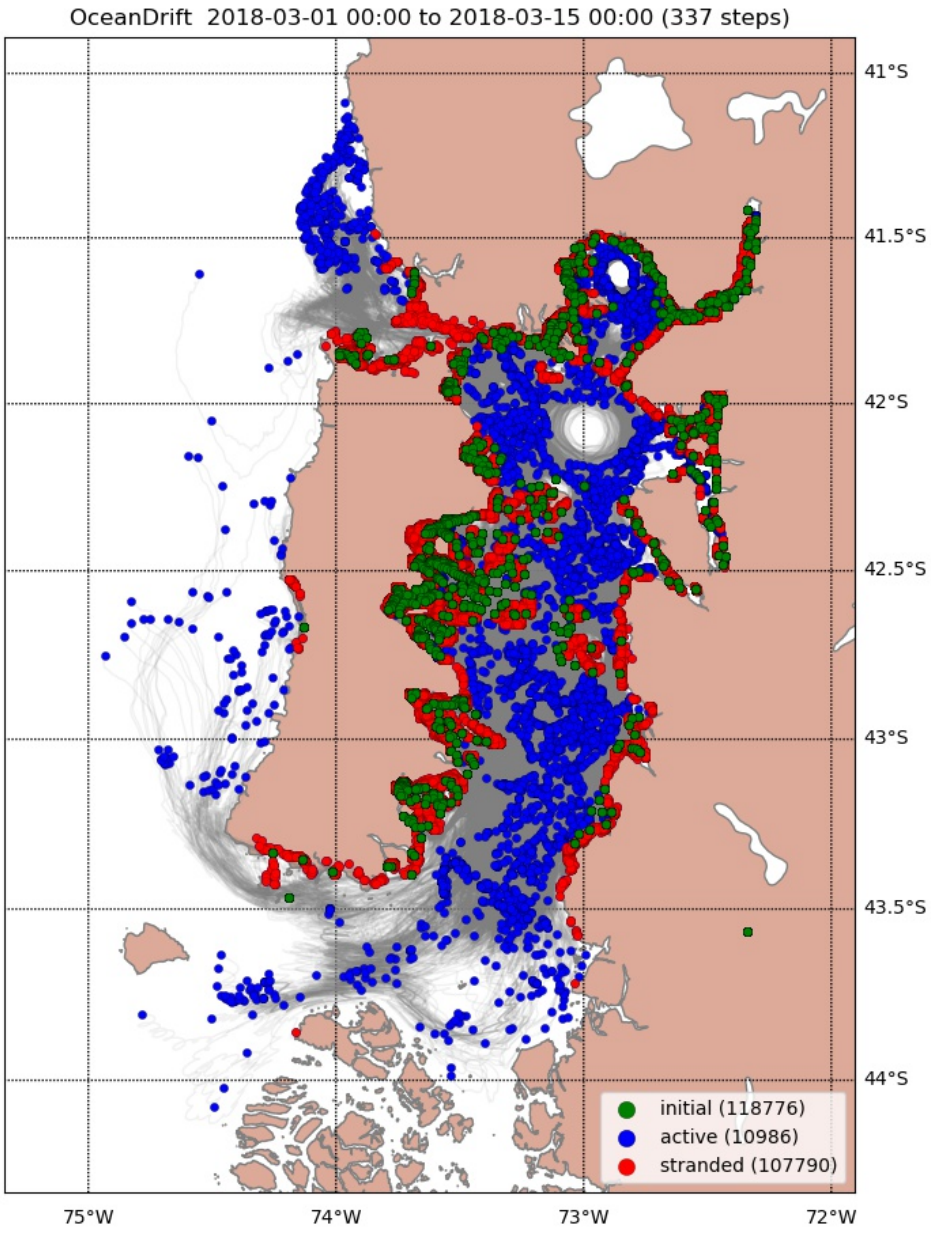

Figura 2.5: Surface particle trajectories simulated with the OpenDrift model by Allel (2020) for a 15-day period in March 2018. The results show circular dispersion patterns in the Gulf of Ancud, suggesting the presence of an eddy-like surface circulation. Similar patterns were later reported by Allel (2020) for other months of the year.

Oceanic eddies are rotating structures that redistribute momentum, heat, and tracers, acting as key agents in the ocean's energy and mass balance. While most studies focus on

mesoscale eddies in the open ocean, recent research highlights that similar vortical structures develop in semi-enclosed basins, where their generation and persistence are primarily controlled by wind stress, tides, density gradients, and topographic constraints rather than large-scale currents.

In semi-enclosed systems such as gulfs, fjords, and inland seas, numerical and observational studies have shown that wind and tidal forcing can induce surface eddies and recirculating cells that modulate water exchange between sub-basins. For instance, in the Gulfs of Patras and Corinth, the interaction between wind and tide generates energetic eddies that govern exchange flows (Aspioti and Fourniotis, 2025), while wind-driven modeling in the Caspian Sea revealed the formation of anticyclonic eddies induced by persistent surface forcing (Mofidi and Rashidi Ebrahim Hesari, 2018). Topographic effects are also critical: idealized simulations in the Gulfs of Oman and Aden demonstrate that bathymetry and mesoscale interactions can produce intense submesoscale vortices dominating local transport processes (Morvan et al., 2019).

At larger scales, reanalyses of the Mediterranean Sea show that mesoscale eddies and winter mixing control water mass exchanges and deep-water formation (Barral et al., 2024; Gačić and Bensi, 2020). Earlier theoretical works—such as baroclinic and box-type models—laid the foundations for understanding eddy viscosity and turbulent exchange in enclosed basins (Özhan and Balas, 2003), whereas recent studies demonstrate that steady wind forcing alone can generate secondary circulation even in narrow basins, challenging classical Rossby-radius constraints (Amadori et al., 2020).

In this context, the Chiloé Inland Sea (CIS) presents a particularly favorable environment for eddy formation due to its complex topography, strong tidal currents, freshwater inputs, and seasonally variable winds. Understanding how these local forcings interact to generate and sustain recirculating structures is essential to describe the mesoscale variability observed in the Gulf of Ancud and its role in regional exchange and mixing.

Bathymetry also acts as an important forcing agent in the generation of eddies, especially through the interaction of ocean currents with seafloor features such as submarine canyons, sandbanks, and steep slopes. These interactions can induce ageostrophic forces that generate cyclonic eddies and favor the exchange of water masses between the continental shelf and the slope (Connolly and Hickey, 2014). Laboratory experiments have shown that coastal currents produce eddies when interacting with steep bathymetric slopes, depending on the relationship between current width and bottom curvature (Sutherland and Cenedese, 2009).

Wind stress is another physical forcing that contributes to the formation of eddies. These structures originate due to interactions between ocean currents and surface winds, which generate pressure variations and dynamic forces in the water column. For example, in Massachusetts Bay, an anticyclonic eddy formed due to the pressure gradient generated by the Ekman transport induced by strong winds, separating a coastal current from its original trajectory (Jiang et al., 2011). However, wind can also reduce the intensity of an eddy. In the Gulf of Mexico, mixing instabilities have been observed in a warm core eddy due to the

reduction of potential vorticity by heat fluxes and wind stresses aligned with geostrophic currents (Pérez et al., 2022).

Recent studies have revealed a direct relationship between wind stress and eddy kinetic energy (EKE), particularly in semi-enclosed basins where wind forcing and topographic constraints interact. In the western Mediterranean, local and non-local energy transfer between mean flow and eddies was found to be controlled by topography and wind variability (Capó et al., 2019). Similarly, in the Caribbean Sea, spatial and temporal patterns of EKE were shown to correlate with seasonal winds and the migration of the Intertropical Convergence Zone (López-Álzate et al., 2022). Numerical experiments in enclosed basins further indicate that the barotropic response to uniform winds depends on the magnitude and vertical profile of turbulent viscosity, influencing inertial oscillations and upwelling zones (Wang et al., 2001). These findings suggest that variations in wind stress not only trigger eddy formation but also modulate their kinetic energy and persistence through dynamic coupling with stratification and bathymetric features.

Residual tidal eddies are permanent or semi-permanent structures formed by the nonlinear interaction of tides with topography, or by frictional and rotational effects (Coriolis). Unlike tidal eddies, they do not oscillate with the tidal cycle, but reflect the cumulative effect of tides. In addition, freshwater flows into the ocean also generate eddies through the interaction of freshwater plumes with ocean currents. A significant case is the interaction of the Amazon plume with the rings of the Northern Brazil Current (NBC), which generates mesoscale eddies capable of redistributing low salinity and modifying heat exchanges between the ocean and the atmosphere (Coadou-Chaventon et al., 2024). The main mechanisms include baroclinic and barotropic instabilities, induced by density differences due to salinity and wind. These mechanisms create favorable conditions for the generation of eddies in the CIS, where intense tidal currents and freshwater inputs interact with complex topography. However, whether the observed eddy corresponds to a residual tidal feature, a wind-driven structure, or another mechanism remains to be determined in this study.

In some regions, the occurrence of eddies is a particular feature of the area. An example is eddies in semi-enclosed seas, oceanic formations where water currents rotate in a circular pattern within partially enclosed areas, such as bays, gulfs, or regions surrounded by islands. These eddies are distinguished by their interaction with open water and the physical barriers that limit their full circulation. Their formation is influenced by the interaction between currents, underwater topography, and external forcings such as wind and tide. In the Red Sea and Gulf of Aden, density currents interact with rifts and capes, generating eddies due to barotropic and baroclinic instabilities, which significantly influence the local dynamics of these semi-enclosed regions (Morvan et al., 2020). In the Baltic Sea, vorticity in the eddy cores varies seasonally, with greater intensity and compaction during winter (Vortmeyer-Kley et al., 2019).

The evolution of eddy detection methods has progressed from direct observation to advanced modeling and satellite techniques, expanding the ability to identify eddies ranging from large to submesoscale scales. Initially, eddies were recognized only to a limited extent

through direct ship observations or anecdotal reports, which restricted detection to large surface structures and provided no insight into their internal dynamics. The use of Synthetic Aperture Radar (SAR) for eddy detection began in the 1970s, particularly after the launch of satellite radar sensors such as Seasat (1978), which enabled the identification of eddies through changes in sea surface roughness caused by velocity gradients and mixing processes associated with these gyres (Redondo Apraiz and Platónov, 2001). Later, the advent of satellite altimetry with missions such as TOPEX/Poseidon (1992) allowed the detection of mesoscale eddies (10–100 km) from sea level anomalies, revolutionizing global eddy monitoring in near real time (Correa-Ramirez and Hormazabal, 2012). These advances also improved detection in coastal and semi-enclosed regions, where eddies are strongly influenced by local bathymetry and coastal dynamics.

With the advent of high-resolution ocean models such as CROCO, it has become possible to explicitly resolve submesoscale structures (<10 km), bridging the gap between satellite observations and in situ measurements. These models complement remote-sensing data by providing a three-dimensional view of circulation and mixing processes, which are especially relevant in semi-enclosed systems where observational coverage is limited.

Although coupled atmosphere–ocean models such as WRF–CROCO have been shown to improve the representation of mesoscale processes, especially through mechanisms like the wind–eddy feedback (or "eddy killing") that transfers kinetic energy from oceanic eddies to the atmosphere (e.g. Renault et al., 2016, 2019), there is currently no direct evidence that this mechanism operates in semi-enclosed basins similar to the Chiloé Inland Sea. Recent studies of regional air–sea coupling in enclosed seas (e.g., the Mediterranean) indicate that surface temperature gradients can modulate wind stability and boundary-layer dynamics (Desbiolles et al., 2021), but these processes differ fundamentally from the mesoscale feedback proposed by Renault et al.

Therefore, the potential influence of wind–eddy coupling in this study area remains speculative. Since the present simulations are uncoupled, the interaction between oceanic eddies and surface winds is not represented, and the "eddy killing" mechanism cannot be assessed here. Consequently, any potential differences between simulated and observed eddy intensity—should they occur—could arise either from the lack of air–sea coupling or from model resolution and subgrid-scale parameterizations. Further analysis would be required to determine their relative importance.

In conclusion, this study aims to characterize, for the first time, the hydrodynamic structure and forcing mechanisms of the eddy observed in the Gulf of Ancud. Using a high-resolution numerical model, we evaluate the relative influence of wind, tides, and bathymetry on its generation and persistence, providing new insight into the mesoscale circulation and exchange processes of the Chiloé Inland Sea.

2.3. Methods

The Coastal and Regional Ocean Community Model (CROCO) (Shchepetkin and McWilliams, 2003, 2005; Debreu et al., 2008) was used to simulate the three-dimensional circulation of the Gulf of Ancud and the surrounding Chiloé Inland Sea. The model solves the primitive equations of ocean dynamics using horizontal curvilinear coordinates and 42 vertical sigma levels, refined near the surface and bottom to accurately represent boundary layers and the interaction between surface and deep waters. Horizontal resolution is 1/72°, providing the spatial resolution necessary to represent mesoscale features such as the observed eddy.

The model domain spans 18° latitude by 8° longitude, encompassing all major channels, fjords, and micro-basins of the region (Fig. 2.3). Bathymetry was constructed from a combination of GEBCO08 data and high-resolution soundings from SHOA, manually corrected to represent small fjords and channels, and smoothed to minimize pressure gradient errors typical of sigma-coordinate models (Haidvogel et al., 2000).

CROCO was forced at the open boundaries with the principal tidal constituents (M2 and S2) (Aiken, 2008), using the TPXO8 inverse solution (Egbert and Erofeeva, 2002), while atmospheric forcing—including wind stress, heat fluxes, precipitation, and radiation—was derived from WRF outputs at 3 km resolution (Skamarock et al., 2019). Freshwater inputs were incorporated as point sources using data from 35 rivers provided by the General Water Directorate (DGA), with monthly variability (IFOP, 2021).

A series of sensitivity experiments were conducted to evaluate the relative role of tides, winds, bathymetry, and freshwater input on the formation and persistence of the Gulf of Ancud eddy. Experiments included configurations with and without tidal forcing, with climatological winds, and with a flattened bathymetry, during both summer (January) and winter (July). Model outputs were saved hourly, discarding the first three days to avoid spin-up effects.

The flat bathymetry experiment imposed a uniform depth of 150 m to evaluate topographic effects, the MOSA bathymetry used the combined SHOA and GEBCO data to represent realistic channels and fjords, and climatological wind experiments employed monthly averaged winds to isolate the effect of wind variability.

Experiment	Tides (M2 & S2)	Wind	Flat Bathymetry	MOSA Bathymetry	Summer	Winter
Summer Control	✓	✓		✓	✓	
Summer Without Tides		✓		✓	✓	
Summer Flat Bathymetry	✓	✓	✓		✓	
Summer Climatological Winds	✓	CLIM		✓	✓	
Winter Control	✓	✓		✓		✓
Winter Without Tides		✓		✓		✓
Winter Flat Bathymetry	✓	✓	✓			✓
Winter Climatological Winds	✓	CLIM		✓		✓

Cuadro 2.1: Details of the Simulations with Forcings in Each Experiment

Validation was performed using sea level data from five coastal tide gauges (SHOA) and ten ADCP deployments (IFOP) across the study area (Fig. 2.6a). Observed and simulated time series were compared using correlation coefficients, root mean square error (RMSE), and scatter index (SI) to assess the model's ability to reproduce tidal dynamics and surface circulation patterns.

The harmonic decomposition is based on representing the sea level variation as a sum of sine waves, each associated with a specific frequency and amplitude corresponding to the main astronomical constituents. Mathematically, sea level $h(t)$ is expressed as:

$$h(t) = Z_0 + \sum_{i=1}^{N} H_i \cos(\omega_i t + \phi_i),$$

where:

- Z_0: Median sea level.
- H_i: Amplitude of the constituent i.
- ω_i: Angular frequency associated with the constituent i.
- ϕ_i: Phase of the constituent i.
- t: Time.

The analysis is carried out using the `t_tide` tool, which adjusts the time series to these sinusoidal components in order to extract the astronomical tides (*harmonic tide*). The difference between the total sea level and this astronomical tide corresponds to the *residual tide*, which includes non-periodic effects such as meteorological, barotropic or local dynamics.

The spin-up duration was determined using two complementary approaches:

1. **Exponential fit:** the domain-averaged kinetic energy (KE) was fitted as

   $$\mathrm{KE}(t) = \mathrm{KE}_\infty + Ae^{-t/\tau},$$

   where KE_∞ is the asymptotic kinetic energy and τ is the e-folding time scale. The spin-up was defined as 3τ (de Freitas Assad et al., 2009; Megann and Storkey, 2021).

2. **Envelope method:** the KE time series was smoothed using a low-pass filter, and the spin-up was defined as the point when the relative change remained below 1 % for a sustained period.

Both methods yielded consistent results, indicating that the model reached dynamical equilibrium after approximately 58 hours from the simulation start (January and July). This cutoff was adopted for all subsequent analyses.

The model outputs provide wind stress over the ocean surface, which was converted into zonal (U) and meridional (V) wind components using the quadratic drag law:

$$U = \sqrt{\frac{\tau_x}{\rho C_D}}, \quad V = \sqrt{\frac{\tau_y}{\rho C_D}},$$

where $\rho = 1{,}225\,\mathrm{kg/m^3}$ is the air density, and $C_D = 0{,}0012$ is the drag coefficient (Large and Pond, 1981) b. From these components, wind speed magnitude and direction were calculated as

$$|\mathbf{U}| = \sqrt{U^2 + V^2}, \quad \theta = \arctan 2(V, U),$$

with θ measured from the east, positive counterclockwise.

Wind stress represents the tangential force per unit area exerted by the wind on the ocean surface due to air–sea friction. The spatial variability of this forcing is characterized by the *wind stress curl*, which measures the rotational component of the wind stress field ($\vec{\tau}$). It is defined as:

$$\mathrm{curl}(\vec{\tau}) = \frac{\partial \tau_y}{\partial x} - \frac{\partial \tau_x}{\partial y},$$

where τ_x and τ_y are the zonal and meridional components of wind stress, respectively. Positive values of the curl indicate cyclonic (counterclockwise) forcing, which tends to promote upwelling and surface divergence, whereas negative values indicate anticyclonic (clockwise) forcing and convergence. The wind stress and its curl were computed from the WRF-derived surface wind fields at 3 km resolution and temporally averaged for January (summer) and July (winter) conditions.

To analyze the residual tidal circulation, the barotropic velocity components (($\bar{u}$) and ($\bar{v}$)) were extracted from the CROCO hourly outputs. Residual (time-averaged) velocities were computed by averaging both components over the final 648 model hours, after the spin-up period was discarded to ensure steady conditions. The resulting mean fields were interpolated onto the model's (ρ)-points grid to obtain a consistent spatial representation. The magnitude of the residual current was then calculated as:

$$|U| = \sqrt{\bar{u}^2 + \bar{v}^2}.$$

These residual velocity fields represent the net (non-tidal) circulation driven by the combined effects of tides, winds, and freshwater inputs. Visualization was performed using the m_map and cmocean MATLAB toolboxes, with vector subsampling for clarity and a reference arrow indicating typical current magnitudes.

To analyze the instantaneous tidal velocity field, the barotropic components of the zonal ($\bar{u}$) and meridional ($\bar{v}$) velocities at time step t=541 were extracted from the model outputs. The velocity magnitude was calculated as

$$|U| = \sqrt{\bar{u}^2 + \bar{v}^2},$$

expressed in meters per second (m/s). Velocity vectors were subsampled to reduce visual clutter, and a maximum threshold of 0.3 m/s was applied to filter anomalous or non-representative values. The fields were visualized using Mercator-projected maps generated with the M_Map toolbox in MATLAB, employing the cmocean("speed") color palette and including a reference arrow indicating a speed of 0.1 m/s.

In order to complement the analysis of the residual circulation and isolate the oscillatory tidal component, an additional harmonic decomposition of the barotropic velocity field was performed. To quantify the tidal component of the circulation, the barotropic velocities ($\bar{u}$ and $\bar{v}$) from the hourly CROCO outputs were decomposed harmonically into their principal semidiurnal constituents (M2 and S2). The analysis was performed at each horizontal grid point by fitting the time series of $\bar{u}$ and $\bar{v}$ to a least-squares model of the form

$$U(t) = A_{M2}\cos(\omega_{M2}t) + B_{M2}\sin(\omega_{M2}t) + A_{S2}\cos(\omega_{S2}t) + B_{S2}\sin(\omega_{S2}t),$$

where ω_{M2} and ω_{S2} are the angular frequencies of the M2 and S2 tidal constituents, respectively. The fitted coefficients were then used to reconstruct the harmonic tidal velocity fields u_{tide} and v_{tide} at each grid point.

The resulting barotropic tidal currents were interpolated to the ρ-points of the model grid to obtain a spatially consistent field. From these reconstructed components, the root-mean-square (RMS) tidal velocity magnitude was computed as

$$U_{\text{RMS}} = \sqrt{\langle u_{\text{tide}}^2 + v_{\text{tide}}^2 \rangle_t},$$

representing the mean kinetic energy associated with the semidiurnal tidal cycle.

Visualization of U_{RMS} and the corresponding tidal vectors was performed using the `m_map` and `cmocean` MATLAB toolboxes. Vectors were subsampled for clarity, and a magnitude threshold was applied to mask spurious or weak tidal regions ($|U_{\text{RMS}}| < 0{,}5$ m s^{-1}). The

resulting maps highlight the spatial variability of the tidal current intensity and direction across the Gulf of Ancud.

2.4. Results

ADCP data from fifteen locations were used (Fig. 2.6a) to evaluate the modeled tidal currents. Tidal current ellipses were calculated for the two dominant semidiurnal components (M2 and S2). In addition, the semi-major axes and amplitudes of M2 and S2 estimated for sea level were compared (Figure 2.6b). The RMSE of the amplitude fitted to all sea level records was 34 cm for M2 (Fig. 2.6b) and 8 cm for S2 (Fig 2.6b), while the dispersion index (SI, normalized RMSE) was lower than 34 % for M2 and 22 % for S2. The model showed excellent overall performance, with very high correlations (r = 0.98 for M2 and r = 0.96 for S2), indicating that it adequately reproduces the shape of the variances of both components. However, for M2, the RMSE of 0.34 m and the SI of 34 % reflect significant discrepancies in amplitudes, suggesting that improvements could be made by adjusting the resolution, friction parameterization, or boundary forcing. In contrast, S2 presents a better fit, with an RMSE of 0.08 m and an SI of 21.98 %, indicating greater accuracy in the representation of their amplitudes. Although the overall performance is robust, the model could benefit from adjustments to improve the accuracy in M2, and the inclusion of minor tidal components could help capture nonlinear interactions and more realistically represent the dynamics of the studied area.

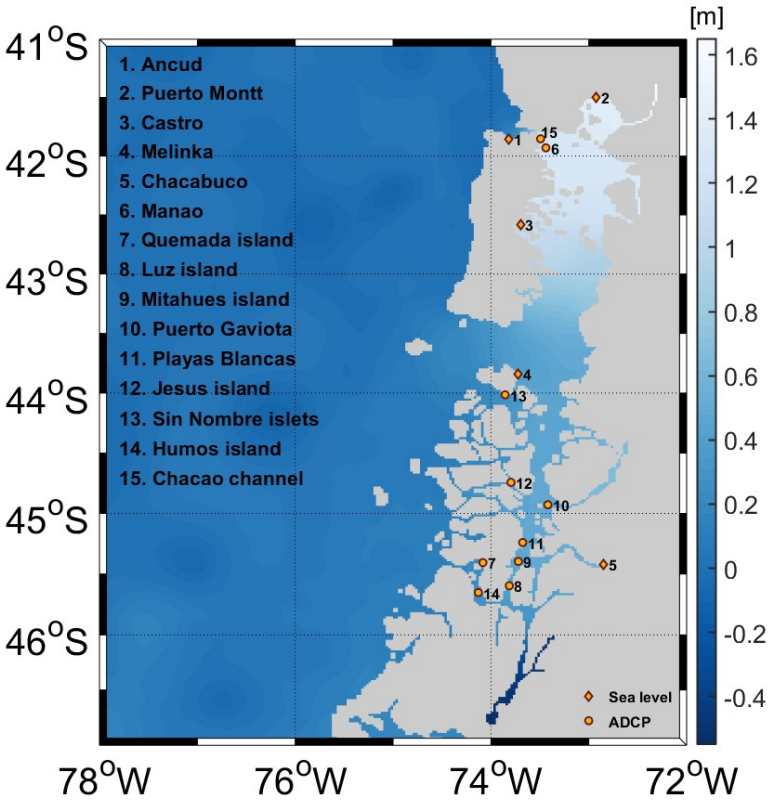

(a)

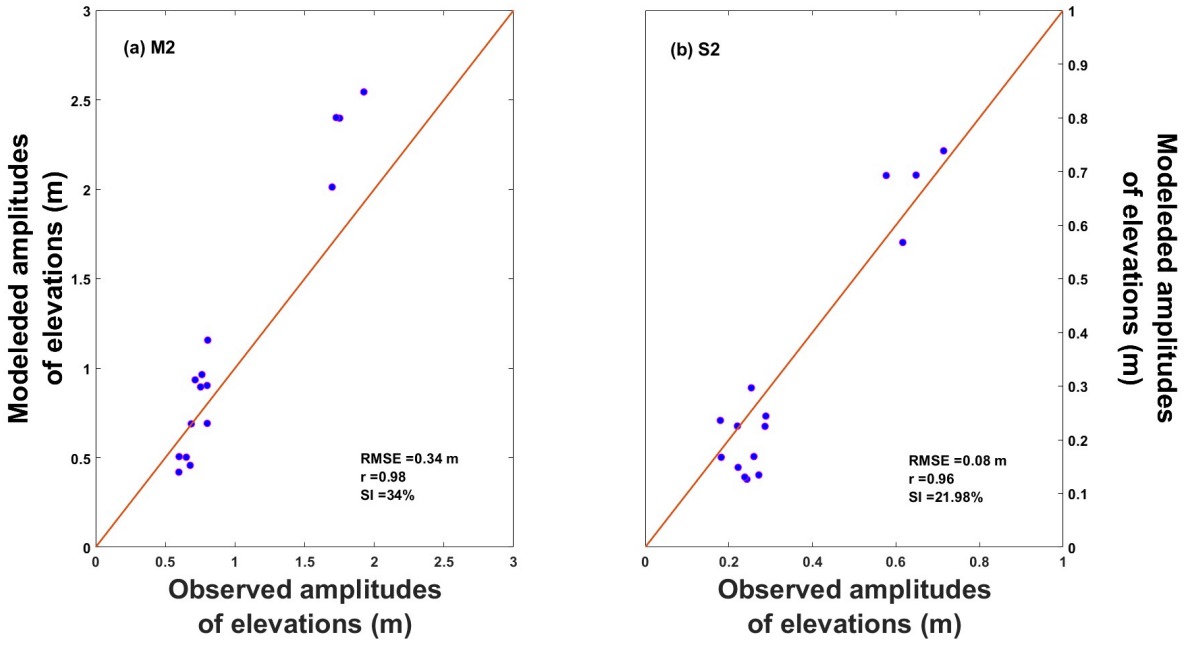

(b)

Figura 2.6: 2.6a: Map of the study area showing where sea level data were collected. Diamonds indicate areas where tide gauges were used, while circles indicate areas where ADCP was used. 2.6b: Scatter plot comparing model-derived sea elevation data with observed data, accompanied by statistical results summarizing the comparison between the two data sets.

The spin-up analysis was carried out by monitoring the temporal evolution of the domain-averaged kinetic energy (KE) until reaching a quasi-stationary state. Figure 2.7 shows the raw and low-pass filtered KE, along with its envelope. The stabilization of the envelope was used as an objective criterion to identify the end of the spin-up period, indicating when the model dynamics reached equilibrium. According to the envelope criterion, the spin-up stabilized approximately 2.4 days after the start of the simulation, whereas the exponential adjustment (3τ) yielded a shorter estimate of about 1.5 days. Since the envelope method provides a more conservative estimate that accounts for oscillatory behavior, it was adopted as the recommended spin-up duration, ending 58 hours after the simulation began. Hence, model outputs after 58 hours are considered reliable for subsequent analysis.

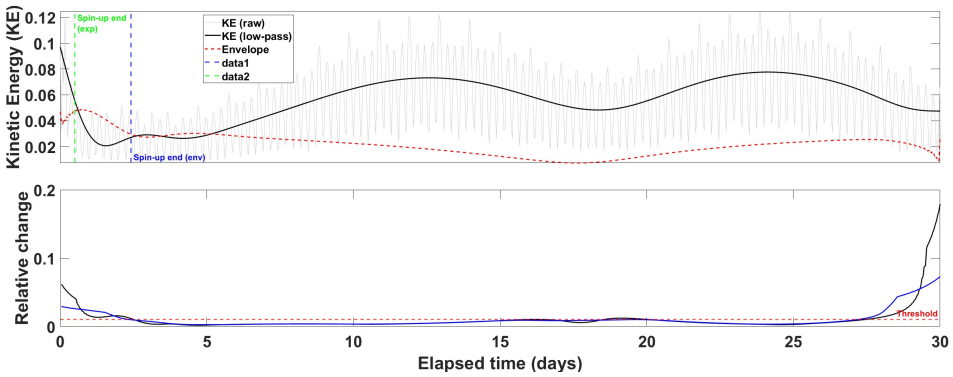

Figura 2.7: Temporal evolution of the domain-averaged kinetic energy (KE) during the spin-up period. The gray line shows the raw KE signal, the black line represents the low-pass filtered KE, and the red dashed line indicates its envelope. The vertical blue and green dashed lines correspond to the spin-up end estimated by the envelope and exponential (3τ) criteria, respectively.

Fig. 2.8 shows the wind speed and direction over the simulated months at each station studied. Since the model provides the wind stress over the ocean surface as output, we converted these stresses into wind speed components using the quadratic drag law.

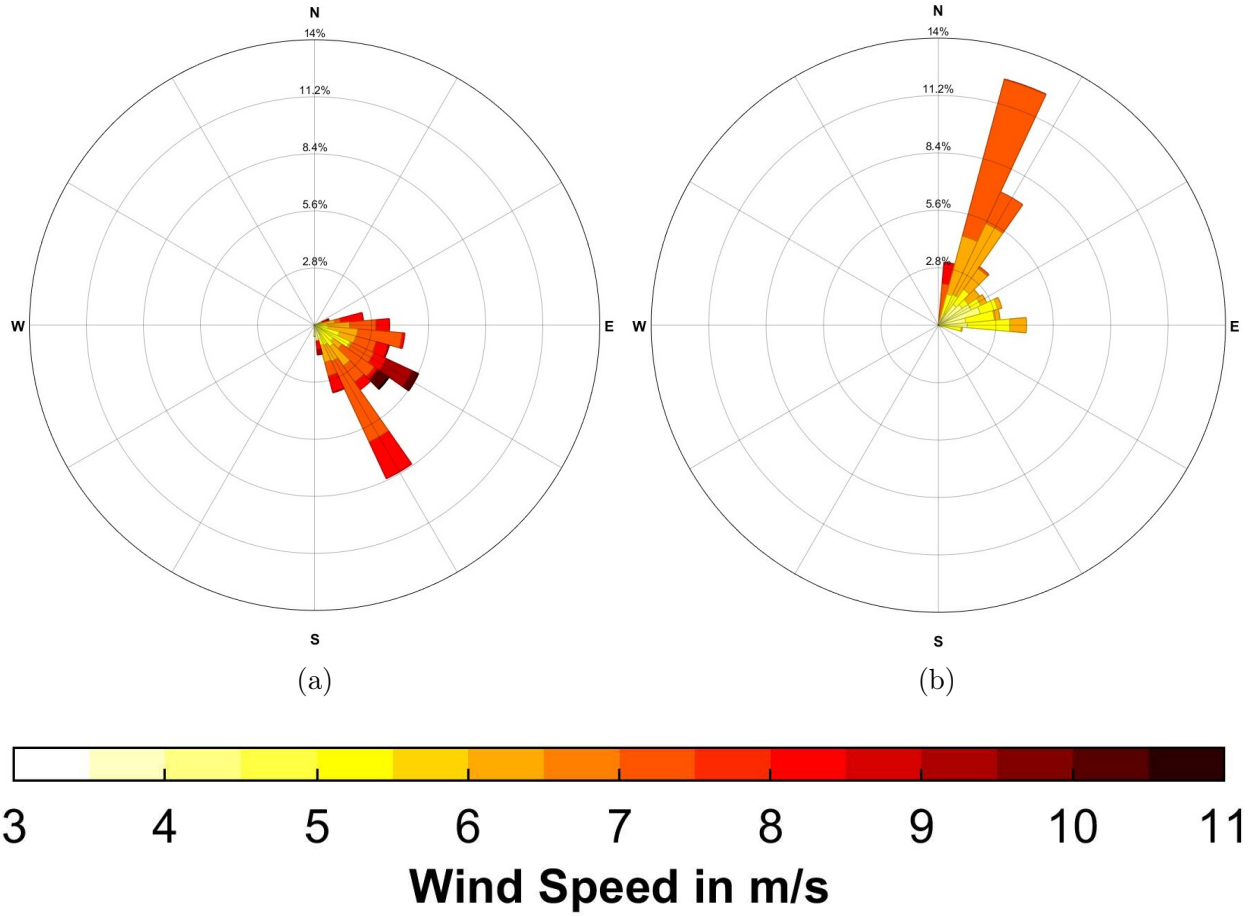

Figura 2.8: Wind directions and magnitudes 2.8a Winter. 2.8b Summer.

In winter (Fig. 2.8a), winds blow predominantly toward the northwest, originating from the southeast. The strongest winds reach intensities between 10 and 11 m/s, reflecting the dominance of a persistent southeasterly regime. The most frequent wind direction also corresponds to southeasterly flow, with mean speeds of approximately 8 m/s, indicating a consistent and well-defined pattern of winds driving surface circulation toward the northwest.

In contrast, during summer (Fig. 2.8b), winds predominantly blow from the northeast toward the southwest. The most frequent and strongest winds come from a direction slightly east of north, reaching maximum speeds of approximately 8 m/s.

The average wind stress during winter is approximately 5 N/m^2, oriented predominantly eastward with a slight southward inclination. The wind stress curl reaches its minimum value (–3.6 N/m^3) in the transition zone between the Gulf of Ancud and the Gulf of Corcovado, increasing slightly (–3.2 N/m^3) toward the central Gulf and forming a semicircular gradient

that weakens toward the coasts (–0.4 N/m^3).

In summer, wind stress directions shift toward the northeast, maintaining similar magnitudes (≈5 N/m^2). The curl minimum (–5.5 N/m^3) occurs again near the Ancud–Corcovado transition, with higher intensities extending southwestward toward the Chacao Channel and decreasing toward the Reloncaví Sound.

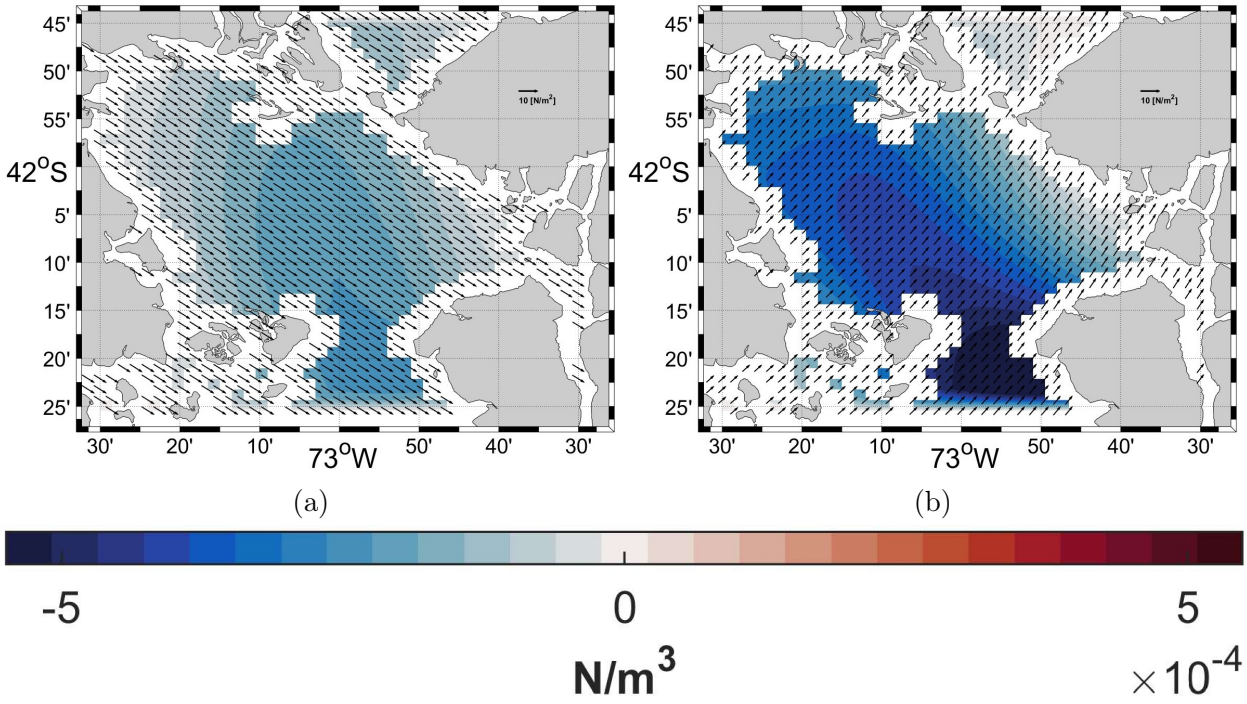

Figura 2.9: The color bar indicates the average monthly wind stress curl. The vectors represent the monthly average wind stress. 2.9a Winter. 2.9b Summer.

In summer, the wind stress directions shift to the northeast, with an average value of 5 N/m^2 throughout the study area. In this case, the wind stress curl also reaches its minimum value in the transition between the Gulf of Ancud and the Gulf of Corcovado, with approximately $-5{,}5\,\mathrm{N/m^3}$. During this season, a series of more intense values is observed extending toward the southwest, from the Gulf of Corcovado towards the Chacao Channel, where the highest curl intensities are found. From this region, the curl gradually decreases towards the coasts, with areas with lower intensity being those located to the northeast, particularly in the Reloncaví Sound.

Figures 2.10 show the tidal velocities obtained from the harmonic decomposition of the barotropic currents. Figure 2.10a represents the winter conditions, where the vectors indicate the direction and magnitude of the tidal velocities, while the color background represents the velocity field magnitude. In the Gulf of Ancud, these tidal velocities are relatively weak, whereas stronger tidal currents are observed along the boundaries, particularly in the transition between the Comau Fjord and the Gulf of Ancud, between the Reloncaví Sound and the

Gulf of Ancud, in the Chacao Channel, and in the passages connecting the Gulf of Ancud with the Gulf of Corcovado. Within the Gulf of Ancud itself, tidal velocities are generally lower and predominantly directed southward.

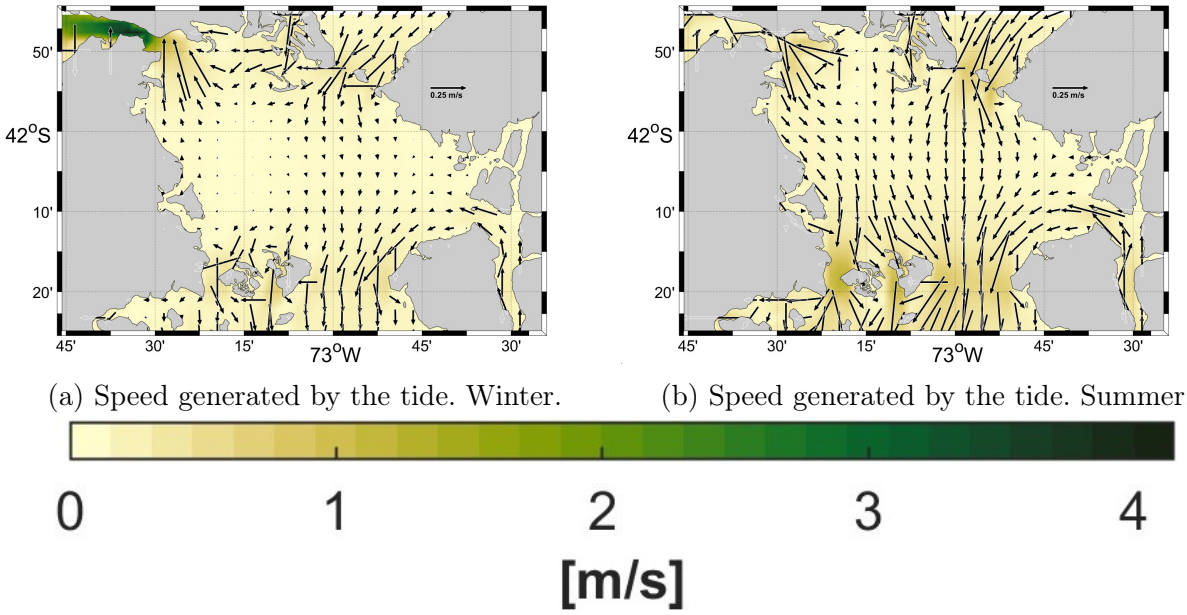

(a) Speed generated by the tide. Winter.

(b) Speed generated by the tide. Summer.

Figura 2.10: Tidal velocities obtained from the harmonic decomposition of the barotropic velocity. Vectors represent the tidal velocity direction and intensity, while the color field shows the magnitude of the tidal velocity. (2.10a) Winter. 2.10b Summer.

Figure 2.10b shows the tidal velocities during the summer conditions. In this case, the Gulf of Ancud exhibits slightly higher velocities compared to the winter scenario, although still weaker than those observed in the connecting passages, the Chacao Channel, and the Comau Fjord. The tidal flow within the Gulf of Ancud remains mostly directed toward the south.

Figures in 2.11 show the residual tidal velocity fields, where the vectors represent the direction and intensity of the residual velocities, and the color field indicates their magnitude. In winter (2.11a), a cyclonic eddy can be observed in the center of the Gulf of Ancud, similar to the one seen later in the surface velocity field of the winter control simulation. In summer (2.11b), a dipole structure is evident in the center of the Gulf of Ancud, with a cyclone to the west and an anticyclone to the east, resembling the pattern observed in the surface velocity field of the summer control simulation.

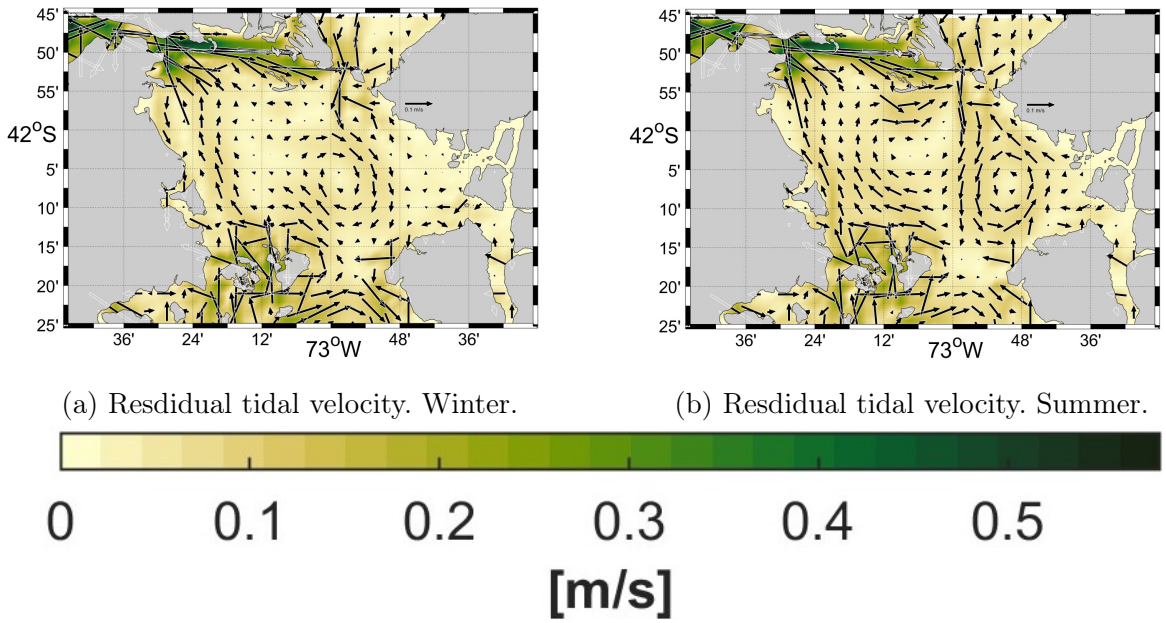

(a) Resdidual tidal velocity. Winter.

(b) Resdidual tidal velocity. Summer.

Figura 2.11: Residual tidal velocities obtained from the harmonic decomposition of the barotropic velocity. Vectors indicate the direction and magnitude of the residual tidal currents, while the color field represents the residual tidal velocity magnitude. (2.11a) Winter. (2.11b) Summer.

Figure 2.12a represents the harmonic decomposition of the tides using the time series analysis extracted from the model. The black line represents the sea level observed by the model (*total tide*), the green line corresponds to the *astronomical tide*, obtained from the harmonic analysis, and the red line shows the *residual tide*, calculated as the difference between total tide and astronomical tide.

Figure 2.12b shows the spatial location of the extraction point of the analyzed time series, highlighted with a marker on a map representing the spatial field of the *residual tide* in time 541. This graph illustrates the surface distribution of the residual tide in the study domain, highlighting spatial patterns that may be related to local phenomena, such as bottom topography, interaction with currents or external forcings.

The analysis of the eddies resulting from each experiment is presented in two types of graphs, placed side by side (Figs. 2.13 and 2.14). One is a surface graph showing current velocities at 10 m depth. This depth was selected because, in winter, the first few meters do not exhibit a consistent pattern due to surface turbulence caused by more intense vertical mixing resulting from less stratification and variable wind action. After 10 meters, the currents stabilize as the mixing forces decrease with depth. In addition, this graph includes sea level anomalies, since these are associated with eddies and the direction of their rotation: cyclonic eddies have low pressure cores because of the ascent of cold and dense water from greater depths, whereas anticyclonic eddies, being associated with warmer and less dense water in the core, present positive sea level anomalies and lower surface pressure.

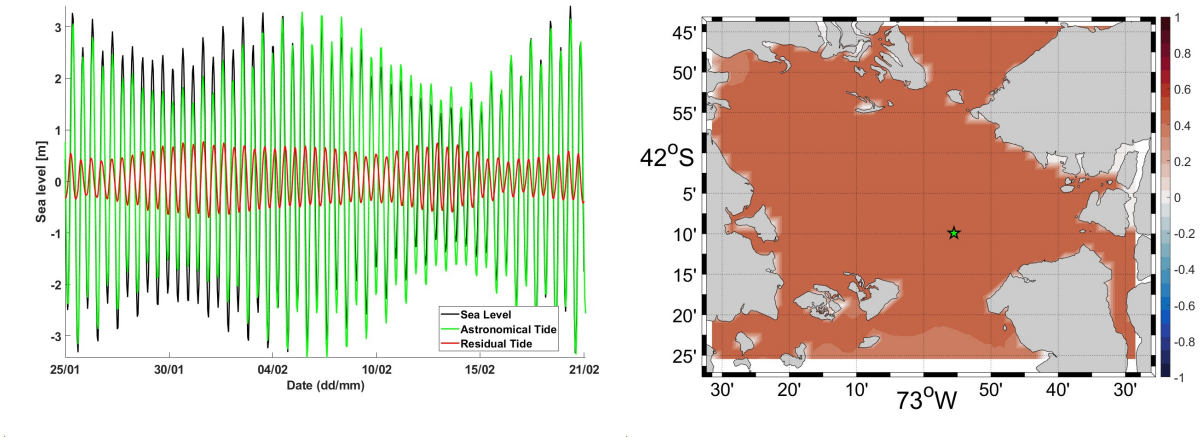

(a) (b)

Figura 2.12: 2.12a Harmonic tidal decomposition: visualized tide (black), astronomical tide (green), residual tide (red). 2.12b Extraction point of the analyzed tide.

Next to the horizontal graph, vertical north-south sections are included (42°25' at 41°45' S) passing through the center of an eddy identified in the surface currents. These sections plot zonal velocities to observe how the eddy affects the water column. The green line on the horizontal plot indicates the location of the transect.

In the circulation of the summer control case, shown in Fig. 2.13a, the formation of a dipole can be observed in the main basin of the Gulf of Ancud. This dipole consists of a cyclone in the western zone, with a diameter of 28.5 km, and an anticyclone of 27 km diameter located in the center of the gulf. The vertical section plotted at 72°51' West (Fig. 2.13c) shows that, in the southern part of the transect, zonal velocities are oriented eastward from the topography of the main basin towards its center. These velocities are most intense in the first 100 meters and remain constant below this depth. In the northern zone, velocities are oriented westward, with greater intensity in the first 75 meters and an increase near the mainland. These velocities gradually decrease with depth, although they do not completely disappear. In summary, currents throughout the water column are westward.

In the experiment with no summer tides (Fig. 2.13b), a cyclone is identified in the center of the Gulf of Ancud with a diameter of 30 km, and an anticyclone of 25 km to the southwest of the basin. In the transition zone towards the Corcovado Gulf, another anticyclone of 27 km in diameter appears. The transect carried out at 72°57' West (Fig. 2.13d) crosses the cyclone and picks up the northern portion of the anticyclone to the south. In the southern part of the basin, velocities are westward, reaching up to 20 cm/s in the first 100 meters and remaining constant with depth. In the northern zone, velocities are oriented toward the east, being more intense at surface levels, although lower in magnitude than those in the southern sector.

In Fig. 2.13e, which corresponds to the experiment with modified summer bathymetry,

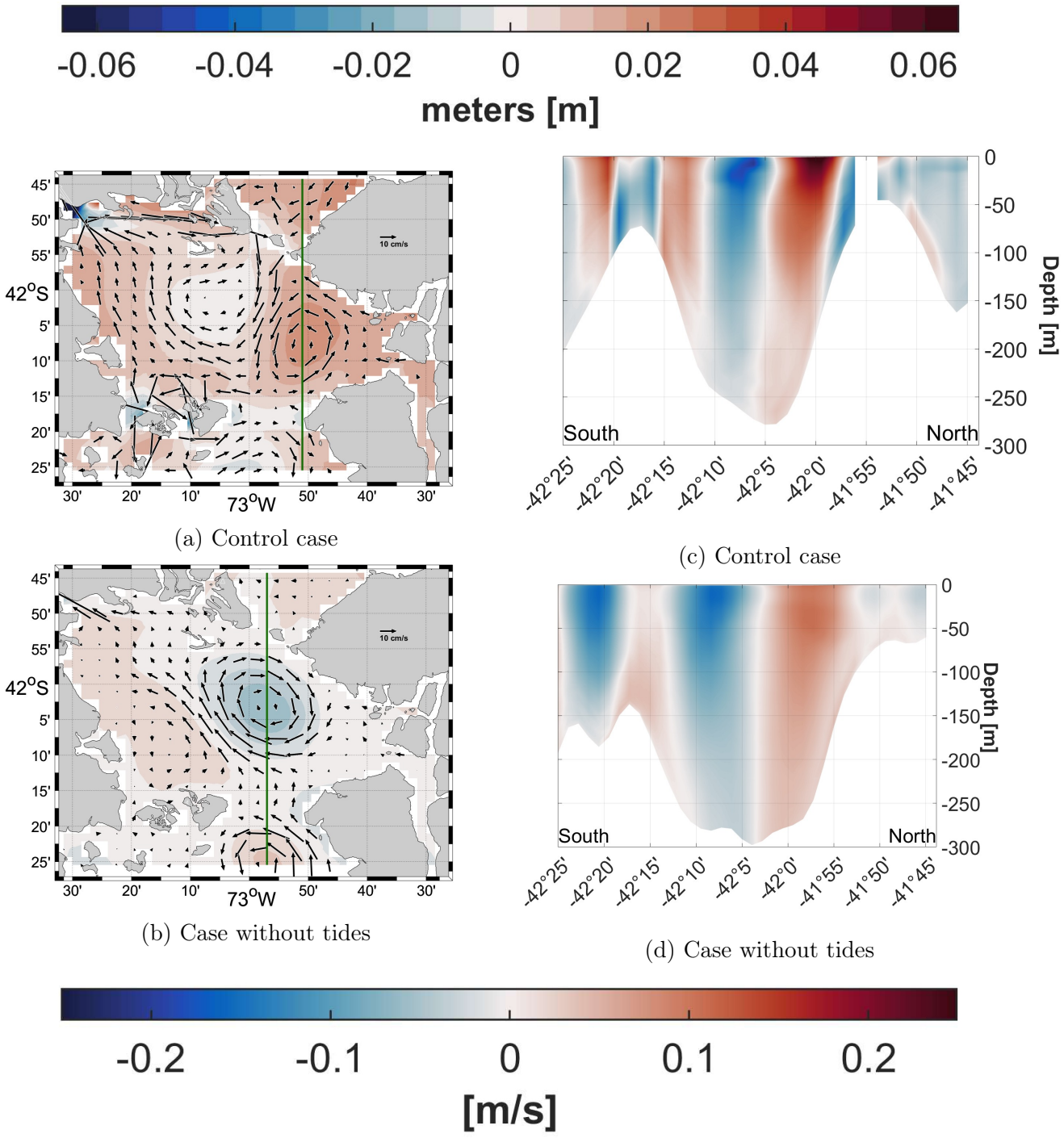

(a) Control case

(b) Case without tides

(c) Control case

(d) Case without tides

Figura 2.13: Winter experiments. (a,b) show sea level anomalies with surface currents velocities, and (e,f) zonal velocity transects for the control and no-tide cases.

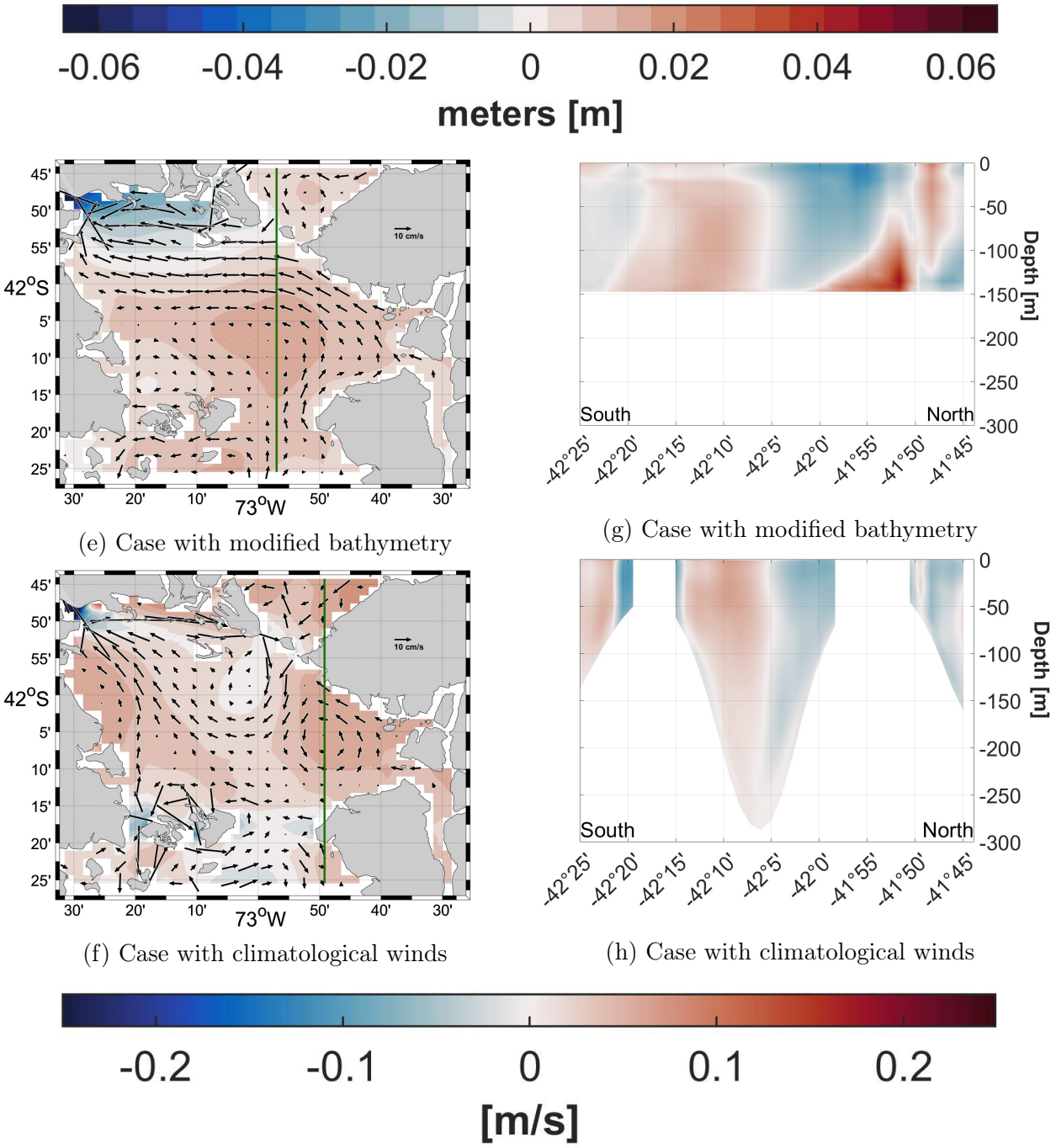

(e) Case with modified bathymetry

(g) Case with modified bathymetry

(f) Case with climatological winds

(h) Case with climatological winds

Figura 2.13: Continuation of Figure 2.13. (c,d) show sea level anomalies with surface currents velocities, and (g,h) zonal velocity transects for the modified-bathymetry and climatological-wind cases.

three eddies are observed: an anticyclone of 16 km in diameter in the Reloncaví Sound, another anticyclone of 24 km in the center of the Gulf of Ancud and a cyclone of 18 km to the southwest. The transect traced at 72°57' West (Fig. 2.13g) passes through these anomalies. In the vertical section, velocities in the south of the basin are directed eastward, while in the north they are oriented westward, reflecting a typical anticyclone pattern. At the surface, the velocities are close to zero, and in the first 5 meters the northerly currents invade the westward-facing water column, which explains why the spin is not perceptible at the surface.

In the experiment with climatological summer winds, the surface current velocities (Fig. 2.13f), surface velocities show three eddies in the study area: a 10 km cyclone in the Reloncaví Sound, a 20 km cyclone in the northern part of the Gulf of Ancud, near Paso Queullín, and a 26 km anticyclone to the east of the cyclone. The transect traced at 72°50'24" West (Fig. 2.13h) shows that in the southern zone, westward velocities are strongest in the first few meters, but decrease significantly after 100 meters and stop near 150 meters. In the northern zone, westward velocities are strongest in the first 50 meters, decrease gradually up to 100 meters, and increase slightly near 200 meters. A small eastward current appears attached to the topography above 150 meters. This pattern indicates an anticyclone that covers the entire water column, although it is not very intense.

The formation of three eddies can be seen in the circulation of the winter control case, seen in Fig. 2.14a: an anticyclone near the Chacao Channel with a diameter of 13 km, another anticyclone to the east of the first, with a diameter of 18 km, and a cyclone in the center of the basin with a diameter of 37 km. A transect was drawn at 72°57' West (Fig. 2.14c), where it can be seen that, in the southern part of the Gulf, the velocities in the first meters are directed toward the east, especially near the southern limit of the basin. However, at greater depth, the velocities change direction towards the west, with a core of maximum intensities at 100 meters depth. These velocities gradually decrease beyond 100 meters, without reaching zero. In the deep zone, between 200 and 250 meters, a small display of eastward velocities can be distinguished, located next to the seamount.

In the winter experiment without tides (Fig. 2.14b), an anticyclone can be identified near the Chacao Channel with a diameter of 27 km, another anticyclone south of Paso Queullín with a diameter of 23 km, and a cyclone in the center of the basin with a diameter of 21 km. The transect, drawn at 72°57' West (Fig. 2.14d), shows that, in the southern zone, surface velocities are almost imperceptible. However, from a depth of 5 meters, a water column with westward velocities is observed, although with low intensities. Near the submarine topography in this zone, there is a peak of intensity in the westward velocities. In the northern zone, surface velocities are more intense, reaching their maximum magnitude around 50 meters depth. All column velocities in this region are directed eastward, with a progressive decrease beyond 100 meters. Near 41°55' South, velocities from the surface to 150 meters, upon contact with the seamount, change direction to the west with greater intensity than in the southern part of the basin. These velocities could correspond to the anticyclonic eddy in the north of the basin.

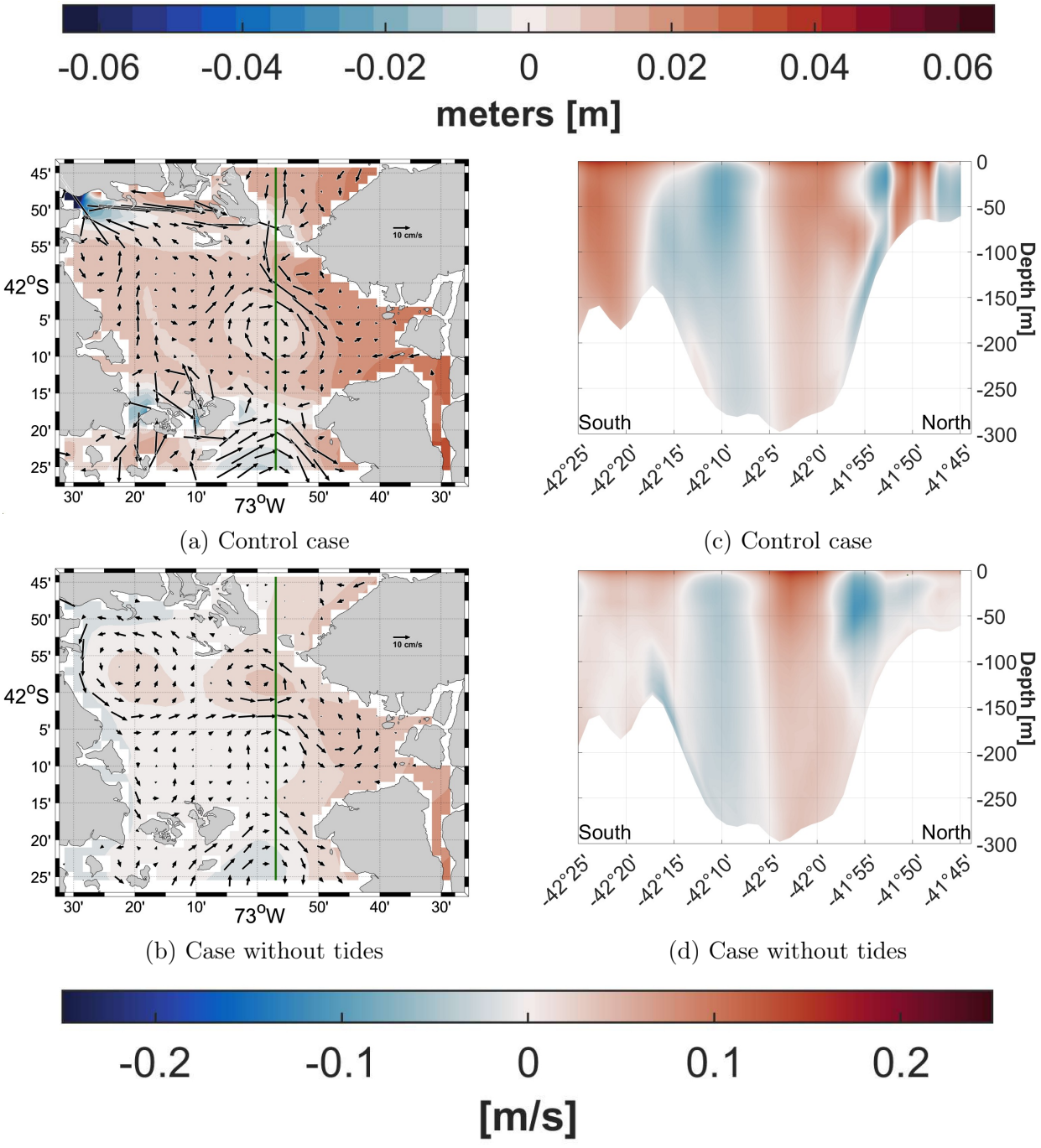

(a) Control case

(c) Control case

(b) Case without tides

(d) Case without tides

Figura 2.14: Winter experiments. (a,b) show sea level anomalies with surface currents velocities, and (e,f) zonal velocity transects for the control and no-tide cases.

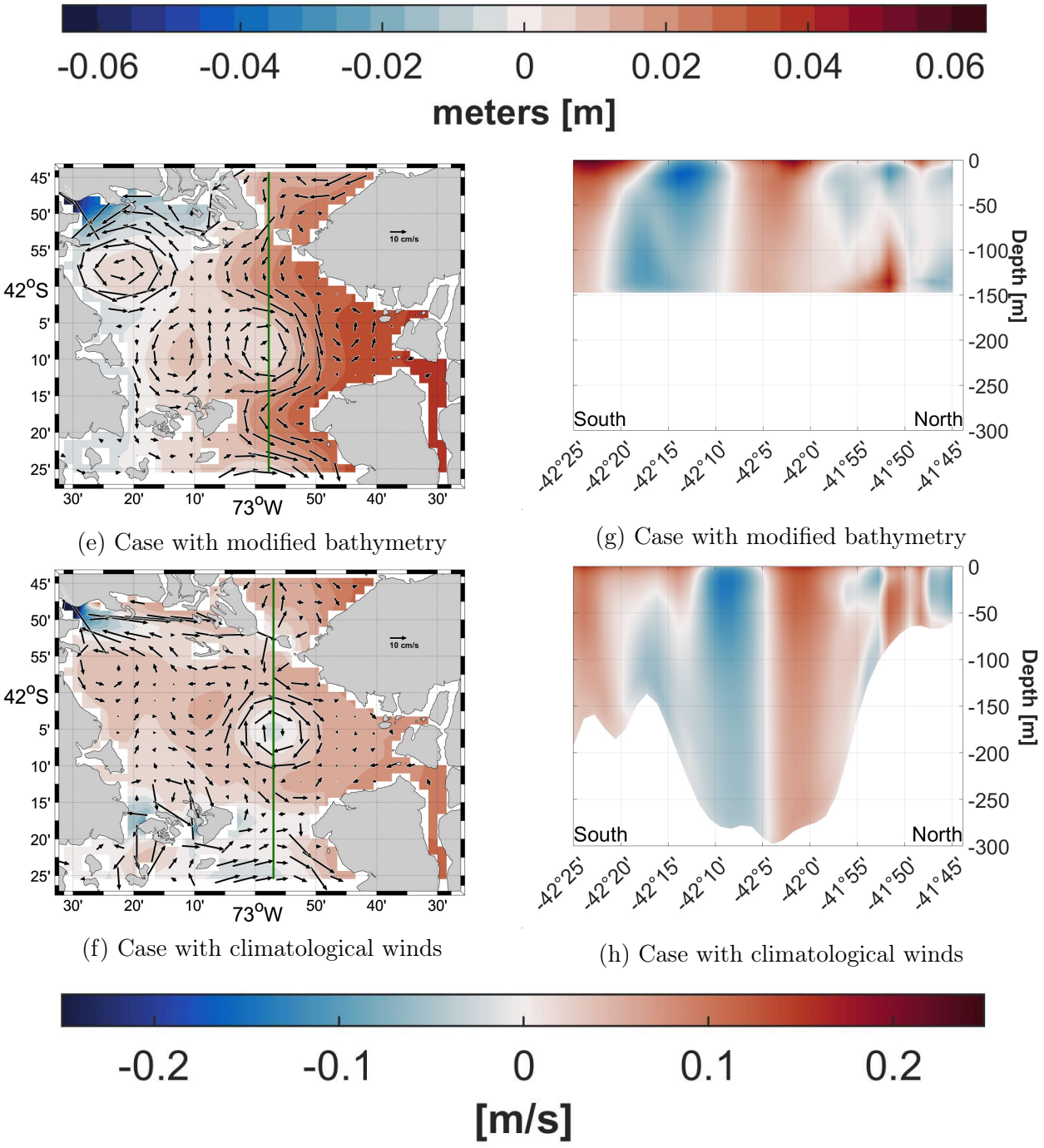

(e) Case with modified bathymetry

(g) Case with modified bathymetry

(f) Case with climatological winds

(h) Case with climatological winds

Figura 2.14: Continuation of Figure 2.14. (c,d) show sea level anomalies with surface currents velocities, and (g,h) zonal velocity transects for the modified-bathymetry and climatological-wind cases.

In Fig. 2.14e, which corresponds to the winter experiment with modified bathymetry, four eddies can be seen: an anticyclone near the Chacao Channel with a diameter of 25 km, another anticyclone to the southwest of the basin with a diameter of 22 km, a cyclone in the center-south of the basin with a diameter of 28 km, and an anticyclone near the Comau Fjord with a diameter of 16 km. We focused on the eddy in the center of the basin, tracing a transect at 72°57'47" West (Fig. 2.14g). In the southern zone, velocities are directed westward, with maximum intensities in the first 25-30 meters, followed by a moderate decrease with depth. A second core of lower intensities is observed between 100 and 150 meters. In the northern zone, velocities are eastward, with a very intense core in the first 20 meters, followed by a second, less intense core down to 75 meters. Velocities decrease progressively towards the bottom, although they do not reach the reduced levels observed in other experiments.

In the experiment with climatological winter winds, surface current velocities (Fig. 2.14f) show three eddies in the study area: a cyclone in the Chacao Channel with a diameter of 16 km and a dipole in the center of the basin, made up of an anticyclone to the west with a diameter of 17 km and a cyclone to the east with a diameter of 21 km. The transect drawn at 72°57' West (Fig. 2.14h) shows that, in the southern zone, velocities are directed westward with maximum intensities in the first 100 meters, followed by a gradual decrease with depth. Throughout the water column, velocities maintain this direction, except near the surface at the seamount, where they change briefly to the east. In the northern zone, an intense eastward core of velocities is observed in the first 75 meters, with a decrease beyond 100 meters without reaching zero. On the northern mound, a display of westward velocities is discernible at depth, followed by eastward velocities at the top, describing a case of a persistent cyclonic eddy throughout the water column.

Experiment (N° of Eddies)	**Type of Eddy**	**Diameter (km)**	**Depth (m)**
Summer Control (2)	Anticyclone	27	282
	Cyclone	28.5	282
Summer Without Tides (3)	Anticyclone	25	–
	Anticyclone	27	180
	Cyclone	20	295
Modified Summer Bathymetry (3)	Anticyclone	16	–
	Anticyclone	24	150
	Cyclone	18	–
Summer Climatological Winds (3)	Anticyclone	26	270
	Cyclone	10	–
	Cyclone	20	–
Winter Control (3)	Anticyclone	13	–
	Anticyclone	18	–
	Cyclone	37	295
Winter Without Tides (3)	Anticyclone	27	–
	Anticyclone	23	–
	Cyclone	21	295
Modified Winter Bathymetry (4)	Anticyclone	25	–
	Anticyclone	22	–
	Anticyclone	16	–
	Cyclone	28	150
Winter Climatological Winds (3)	Anticyclone	16	295
	Cyclone	21	–
	Cyclone	17	–

Cuadro 2.2: Eddy count for each experiment performed. Type of eddy observed (direction of rotation). Diameter of each eddy. The last column represents the maximum depth at which eddy velocities are observed in the cases in which transects were made.

2.5. Discussion

The presence of mesoscale eddies in the Gulf of Ancud was first demonstrated using the results obtained from the MOSA model, a product developed by IFOP based on CROCO. This model has been previously validated by (Artal et al., 2019) and further confirmed in this study, ensuring the reliability of the results. The eddy was identified in the control simulation through multiple indicators, including, circular velocity patterns, and vertical structures inferred from velocity transects. These results are consistent with Lagrangian particle simulations conducted by Allel (2020), who observed circular surface patterns in the Gulf of Ancud while tracking floating debris. While their study did not aim to identify persistent eddies, our high-resolution numerical simulations confirm the presence of a coherent mesoscale structure that persists through the water column.

To better understand the mechanisms responsible for eddy formation, a sensitivity study was conducted. Three experiments were designed for two distinct seasons, winter and summer, in addition to a control simulation. The experiments included: (i) removal of astronomical tides, (ii) a modified bathymetry with a flat bottom at 150 m, and (iii) forcing with climatological winds. Each simulation covered 720 hours, equivalent to a full month in January and July. These experiments aimed to test the hypotheses that (a) the eddy could be tide-driven, as suggested by studies in other semi-enclosed seas (Zimmerman, 1981; Robinson, 1981; Ridderinkhof, 1989), or (b) it corresponds to a topographically influenced, semi-permanent structure, similar to eddies documented in Patagonian gulfs (Tonini and Palma, 2009, 2011).

The results indicate that while the eddy persists across all simulations, its characteristics—position, intensity, size, and number—vary according to the forcing. In summer, a dipole of two large eddies forms in the central basin (cyclone to the west, anticyclone to the east), whereas in winter the eddies are more dispersed, extending towards the Chacao Channel and the Comau Fjord. Experiments without tides showed that the astronomical tide does not play a dominant role in eddy generation in this region, although it can influence their intensity and stability. Conversely, bathymetry and wind forcing modulate the eddy location and shape, highlighting the complex interplay of multiple factors in their formation. This finding challenges previous assumptions about circulation in the Chiloé Inland Sea, which did not account for the presence of persistent mesoscale structures.

Comparisons with similar coastal systems reveal that tidal eddies can dominate in narrow channels or shallow areas (Zimmerman, 1986; Pingree, 1978), but in the Gulf of Ancud the observed structure behaves as a semi-permanent, seasonally modulated feature rather than a classic tidal eddy. Its persistence throughout the year, combined with seasonal variability in intensity and stratification, suggests a dynamical regime controlled by a combination of bathymetric steering and regional circulation rather than tides alone. This insight revises our understanding of the local circulation, indicating that eddies are robust elements that must be considered in studies of transport, mixing, and ecological dynamics within the gulf.

These results suggest several considerations for future research. First, the interaction

between tides, wind, and bathymetry is complex, and their relative contributions could be better quantified through energy and vorticity budgets. CROCO provides access to the terms of momentum and vorticity equations, making it possible to perform such analyses, which have been successfully applied in other semi-enclosed seas (Radko and Marshall, 2004; Tonini and Palma, 2009; Renault et al., 2021). Second, seasonal and interannual variability should be explored, as eddy intensity and structure likely change outside the summer and winter months analyzed here. Third, coupled ocean-atmosphere modeling could provide insights into feedback mechanisms, including the influence of eddies on local wind patterns and heat transport, as observed in other regions (Renault et al., 2021).

Finally, while numerical models like CROCO offer high-resolution insight, limitations remain. Observational validation is still constrained by the scarcity of three-dimensional measurements in narrow coastal areas. Satellite SST and altimetry data have insufficient spatial resolution to capture smaller eddies, and Lagrangian studies provide surface information but cannot fully characterize vertical structures. Integrating numerical simulations with targeted field campaigns will be essential to improve understanding of the Gulf of Ancud's mesoscale dynamics and its ecological implications.

2.6. Conclusions

We can summarize our findings as follows: (i) The simulations carried out demonstrate the capacity of the CROCO model to adequately reproduce the local dynamics of the Gulf of Ancud, although adjustments in spatial resolution and parameterization could improve the representation of the observed processes. (ii) The area in and around the Gulf of Ancud is a zone where eddies are robust elements of the local dynamics. (iii) The eddies identified in the Gulf of Ancud are mesoscale structures whose formation is influenced by the interaction between wind stress, local bathymetry, and regional dynamics. The astronomical tide does not contribute significantly to their generation, as evidenced in the numerical experiments. (iv) Eddies show a marked seasonality, being more intense and stable during the summer due to a greater stratification of the water column. In winter, vertical mixing reduces the intensity and persistence of these structures. (v) These formations affect marine circulation, playing a crucial role in the transport of heat, nutrients, and pollutants within the gulf. Their study is essential to understand the processes of dispersion and for the sustainable management of the marine ecosystem.

Capítulo 3

Conclusiones

Podemos resumir nuestros hallazgos de la siguiente manera: (i) Las simulaciones realizadas demuestran la capacidad del modelo CROCO para reproducir adecuadamente la dinámica local del golfo de Ancud, aunque ajustes en la resolución espacial y en la parametrización podrían mejorar la representación de los procesos observados. (ii) El área del golfo de Ancud y sus alrededores constituye una zona donde los remolinos son elementos robustos de la dinámica local. (iii) Los remolinos identificados en el golfo de Ancud son estructuras de mesoescala cuya formación está influenciada por la interacción entre el esfuerzo del viento, la batimetría local y la dinámica regional. La marea astronómica no contribuye de manera significativa a su generación, como se evidencia en los experimentos numéricos. (iv) Los remolinos presentan una marcada estacionalidad, siendo más intensos y estables durante el verano debido a una mayor estratificación de la columna de agua. En invierno, la mezcla vertical reduce la intensidad y persistencia de estas estructuras. (v) Estas formaciones afectan la circulación marina, desempeñando un papel crucial en el transporte de calor, nutrientes y contaminantes dentro del golfo. Su estudio es esencial para comprender los procesos de dispersión y para la gestión sostenible del ecosistema marino.

Referencias Bibliográficas

Aiken, C. M. (2008). Barotropic tides of the chilean inland sea and their sensitivity to basin geometry. *Journal of Geophysical Research: Oceans*, 113(C8).

Allel, P. (2020). *Dinámica de partículas derivadas de las actividades antrópicas en los fiordos de la Región de Aysén, Chile*. Undergraduate thesis, University of Chile.

Amadori, M., Piccolroaz, S., Dijkstra, H. A., and Toffolon, M. (2020). What makes an elongated lake 'large'? scales from wind-driven steady circulation on a rotating earth. *Journal of Great Lakes Research*, 46(4):703–717.

Andrews, J. T., Syvitski, J. P. M., Burrell, D. C., and Skei, J. M. (1988). Fjords: Processes and products. *Arctic and Alpine Research*, 20(3):375.

Araya-Vergara, J., Vieira, R., and Suárez, M. (2008). El sistema submarino Reloncavi (Nor-Patagonia): Análisis morfoacústico, batimétrico y manto sedimentario reciente. *Ciencia y Tecnología del Mar (Chile)*.

Artal, O., Pizarro, O., and Sepúlveda, H. H. (2019). The impact of spring-neap tidal-stream cycles in tidal energy assessments in the Chilean Inland Sea. *Renewable Energy*, 139:496–506.

Aspioti, A. G. and Fourniotis, N. T. (2025). Numerical study of barotropic circulation in the gulfs of patras and corinth system. *Oceans*, 6(1).

Barral, Q.-B., Zakardjian, B., Dumas, F., Garreau, P., and Beuvier, J. (2024). Assessment of the water mass dynamics over the algero-provencal basin (western mediterranean sea) in the medrys1v2 reanalysis. *Journal of Geophysical Research: Oceans*, 129(12):e2023JC020260. e2023JC020260 2023JC020260.

Capó, E., Orfila, A., Mason, E., and Ruiz, S. (2019). Energy conversion routes in the western mediterranean sea estimated from eddy–mean flow interactions. *Journal of Physical Oceanography*, 49(1):247 – 267.

Chaigneau, A. and Pizarro, O. (2005). Eddy characteristics in the eastern South Pacific. *Journal of Geophysical Research: Oceans*, 110(C6).

Coadou-Chaventon, S., Speich, S., Zhang, D., Rocha, C. B., and Swart, S. (2024). Oceanic fronts driven by the Amazon freshwater plume and their thermohaline compensation at the submesoscale. *Journal of Geophysical Research: Oceans*, 129(7):e2024JC021326.

Connolly, T. P. and Hickey, B. M. (2014). Regional impact of submarine canyons during seasonal upwelling. *Journal of Geophysical Research: Oceans*, 119(2):953–975.

Correa-Ramirez, M. and Hormazabal, S. (2012). Multitaper method-singular value decomposition (MTM-SVD): variabilidad espacio-frecuencia de las fluctuaciones del nivel del mar en el Pacífico suroriental. *Latin American Journal of Aquatic Research*, 40:1039–1060.

Cáceres, M., Valle-Levinson, A., and Atkinson, L. (2003). Observations of cross-channel structure of flow in an energetic tidal channel. *Journal of Geophysical Research: Oceans*, 108(C4).

Dagestad, K. F., Röhrs, J., Breivik, , and Ådlandsvik, B. (2018). OpenDrift v1.0: a generic framework for trajectory modelling. *Geoscientific Model Development*, 11(4):1405–1420. GMD.

de Freitas Assad, L. P., Torres, A. R., Arruda, W. Z., da Silveira Mascarenhas, A., and Landau, L. (2009). Volume and heat transports in the world oceans from an ocean general circulation model. *Brazilian Journal of Geophysics*, 27(2):181–194. https://www.scielo.br/j/rbg/a/M76PfzmfNW4mN4XBLcNzbRq/?lang=enformat=pdf.

Debreu, L., Vouland, C., and Blayo, E. (2008). Agrif: Adaptive grid refinement in fortran. *Computers & Geosciences*, 34(1):8–13.

Desbiolles, F., Alberti, M., Hamouda, M. E., Meroni, A. N., and Pasquero, C. (2021). Links between sea surface temperature structures, clouds and rainfall: Study case of the mediterranean sea. *Geophysical Research Letters*, 48(10):e2020GL091839. e2020GL091839 2020GL091839.

Egbert, G. D. and Erofeeva, S. Y. (2002). Efficient inverse modeling of barotropic ocean tides. *Journal of Atmospheric and Oceanic Technology*, 19(2):183–204.

Gajardo Cortés, C. and Ther Ríos, F. (2011). Saberes y prácticas pesquero-artesanales: Cotidianeidades y desarrollo en las caletas de guabún y puñihuil, isla de chiloé. *Chungará (Arica)*, 43:589–605.

Garreaud, R. and Muñoz, R. C. (2005). The low-level jet off the west coast of subtropical South America: Structure and variability. *Monthly Weather Review*, 133(8):2246–2261.

Gačić, M. and Bensi, M. (2020). Ocean exchange and circulation. *Water*, 12(3).

González-Carrasco, J. and Díaz-Naveaz, J. (2012). Análisis morfológico, estructural y sedimentario de la cuenca del Golfo de Ancud (42 °S; 73 °W) mediante el uso de batimetría multihaz y reflexión sísmica de alta resolución.

Haidvogel, D. B., Arango, H. G., Hedstrom, K., Beckmann, A., Malanotte-Rizzoli, P., and Shchepetkin, A. F. (2000). Model evaluation experiments in the North Atlantic Basin: simulations in nonlinear terrain-following coordinates. *Dynamics of Atmospheres and Oceans*, 32(3):239–281.

Howe, J. A., Austin, W. E. N., Forwick, M., Paetzel, M., Harland, R., and Cage, A. G. (2010). Fjord systems and archives: a review. *Geological Society, London, Special Publications*, 344(1):5–15.

IFOP (2021). Informe final. convenio de desempeño 2020: Desarrollo de sistema de predicción sinóptico de circulación marina, etapa vii. Technical report, Subsecretaría de Economía y EMT. Informe Final.

Iriarte, J. L., González, H. E., and Nahuelhual, L. (2010). Patagonian fjord ecosystems in Southern Chile as a highly vulnerable region: Problems and needs. *AMBIO*, 39(7):463–466.

Jiang, M., Zhou, M., Libby, S. P., and Anderson, D. M. (2011). Dynamics of a mesoscale eddy off Cape Ann, Massachusetts in may 2005. *Deep Sea Research Part I: Oceanographic Research Papers*, 58(11):1130–1146.

Large, W. G. and Pond, S. (1981). Open ocean momentum flux measurements in moderate to strong winds. *Journal of Physical Oceanography*, 11(3):324–336.

Letelier, J. (2010). *Surgencia y Estructuras de Mesoescala frente Chile (18°-42°S)*. Doctoral thesis, University of Concepción.

Letelier, J., Soto-Mardones, L., Salinas, S., Osuna, P., López, D., Sepúlveda, H. H., Pinilla, E., and Rodrigo, C. (2011). Variabilidad del viento, oleaje y corrientes en la región norte de los fiordos patagónicos de chile. *Revista de biología marina y oceanografía*, 46:363–377.

López-Álzate, M. E., Sayol, J.-M., Hernández-Carrasco, I., Osorio, A. F., Mason, E., and Orfila, A. (2022). Mesoscale eddy variability in the caribbean sea. *Ocean Dynamics*, 72(9):679–693.

Martínez, V., Lara, C., Silva, N., Gudiño, V., and Montecino, V. (2015). Variability of environmental heterogeneity in northern Patagonia, Chile: effects on the spatial distribution, size structure and abundance of Chlorophyll-a. *Revista de Biología Marina y Oceanografía*, 50:39–52.

Megann, A. and Storkey, D. (2021). Exploring viscosity space in an eddy-permitting global ocean model: Is viscosity a useful control for numerical mixing? *Journal of Advances in Modeling Earth Systems*, 13(5):e2020MS002263. e2020MS002263 2020MS002263.

Mofidi, J. and Rashidi Ebrahim Hesari, A. (2018). Numerical simulation of the wind-induced current in the caspian sea. *International Journal Of Coastal, Offshore And Environmental Engineering(ijcoe)*, 3(1):67–77.

Morvan, M., Carton, X., L'Hégaret, P., de Marez, C., Corréard, S., and Louazel, S. (2020). On the dynamics of an idealised bottom density current overflowing in a semi-enclosed basin: mesoscale and submesoscale eddies generation. *Geophysical Astrophysical Fluid Dynamics*, 114(4-5):607–630. doi: 10.1080/03091929.2020.1747058.

Morvan, M., L'Hégaret, P., Carton, X., Gula, J., Vic, C., de Marez, C., Sokolovskiy, M., and Koshel, K. (2019). The life cycle of submesoscale eddies generated by topographic interactions. *Ocean Science*, 15(6):1531–1543.

Özhan, E. and Balas, L. (2003). Simulation of water exchange in enclosed water bodies. In Sloot, P. M. A., Abramson, D., Bogdanov, A. V., Gorbachev, Y. E., Dongarra, J. J., and Zomaya, A. Y., editors, *Computational Science — ICCS 2003*, pages 195–204, Berlin, Heidelberg. Springer Berlin Heidelberg.

Pantoja, S., Luis Iriarte, J., and Daneri, G. (2011). Oceanography of the Chilean Patagonia. *Continental Shelf Research*, 31(3):149–153.

Pickard, G. (1971). Some physical oceanographic features of inlets of Chile. *Journal of the Fisheries Board of Canada*, 28(8):1077–1106.

Pingree, R. (1978). The formation of the shambles and other banks by tidal stirring of the seas. *Journal of the Marine Biological Association of the United Kingdom*, 58(1):211–226.

Pérez, J. G. C., Pallàs-Sanz, E., Tenreiro, M., Meunier, T., Jouanno, J., and Ruiz-Angulo, A. (2022). Overturning instabilities across a warm core ring from Glider observations. *Journal of Geophysical Research: Oceans*, 127(4):e2021JC017527.

Radko, T. and Marshall, J. (2004). Eddy-induced diapycnal fluxes and their role in the maintenance of the thermocline. *Journal of Physical Oceanography*, 34(2):372–383.

Rebolledo, L. (2012). Resistencia y cambios identitarios en trabajadores/as del salmón en Quellón. *Polis (Santiago)*, 11:223–239.

Redondo Apraiz, J. M. and Platónov, A. K. (2001). Aplicación de las imágenes SAR en el estudio de la dinámica de las aguas y de la polución del mar Mediterráneo cerca de Barcelona. *Ingeniería del Agua*, 8(1):15–23.

Renault, L., Arsouze, T., and Ballabrera-Poy, J. (2021). On the influence of the current feedback to the atmosphere on the Western Mediterranean sea dynamics. *Journal of Geophysical Research: Oceans*, 126(1):e2020JC016664.

Renault, L., Marchesiello, P., Masson, S., and McWilliams, J. C. (2019). Remarkable control of western boundary currents by eddy killing, a mechanical air-sea coupling process. *Geophysical Research Letters*, 46(5):2743–2751.

Renault, L., Molemaker, M. J., McWilliams, J. C., Shchepetkin, A. F., Lemarié, F., Chelton, D., Illig, S., and Hall, A. (2016). Modulation of wind work by oceanic current interaction with the atmosphere. *Journal of Physical Oceanography*, 46(6):1685–1704.

Ridderinkhof, H. (1989). Tidal and residual flows in the western Dutch Wadden Sea III: Vorticity balances. *Netherlands Journal of Sea Research*, 24(1):9–26.

Robinson, I. S. (1981). Tidal vorticity and residual circulation. *Deep Sea Research Part A. Oceanographic Research Papers*, 28(3):195–212.

Rodrigo, C. (2006). Topografía submarina en canales de la Patagonia norte. *Avances en el conocimiento oceanográfico de las aguas interiores chilenas, Puerto Montt a Cabo de Hornos*.

Saldías, G. S., Sobarzo, M., and Quiñones, R. (2019). Freshwater structure and its seasonal variability off western Patagonia. *Progress in Oceanography*, 174:143–153.

Schneider, W., Fuenzalida, R., Rodríguez-Rubio, E., Garcés-Vargas, J., and Bravo, L. (2003). Characteristics and formation of Eastern South Pacific Intermediate Water. *Geophysical Research Letters*, 30(11).

Shchepetkin, A. F. and McWilliams, J. C. (2003). A method for computing horizontal pressure-gradient force in an oceanic model with a nonaligned vertical coordinate. *Journal of Geophysical Research: Oceans*, 108(C3).

Shchepetkin, A. F. and McWilliams, J. C. (2005). The regional oceanic modeling system (ROMS): a split-explicit, free-surface, topography-following-coordinate oceanic model. *Ocean Modelling*, 9(4):347–404.

Shen, X., Detenbeck, N., and You, M. (2022). Spatial and temporal variations of estuarine stratification and flushing time across the continental U.S. *Estuar Coast Shelf Sci*, 279:1–19. 1096-0015.

Sievers, H. (2008). Water masses and circulation in austral Chilean channels and fjords. *Progress in the oceanographic knowledge of Chilean interior waters, from Puerto Montt to Cape Horn*, pages 53–58.

Sievers, H., Calvete, C., and Silva, N. (2002a). Distribución de características físicas, masas de agua y circulación general para algunos canales australes entre el Golfo de Penas y el Estrecho de Magallanes (Crucero CIMAR-2 fiordos), Chile. *Ciencia y Tecnología del Mar (Chile)*, 25(2):1–43.

Sievers, H., Calvete, C., and Silva, N. (2002b). Distribución de características físicas, masas de agua y circulación general para algunos canales australes entre el Golfo de Penas y el Estrecho de Magallanes (Crucero CIMAR Fiordo 2). *Ciencia y Tecnologia del Mar (Chile)*, 25:17–43.

Sievers, H. A. and Silva, N. (2006). 4.1 masas de agua y circulación en los canales y fiordos australes. *Silva, N., Palma, S.(Eds.), Avances en el conocimiento oceanográfico de las aguas interiores chilenas, Puerto Montt a Cabo de Hornos. Comité Oceanográfico Nacional—Pontificia Universidad Católica de Valparaíso, Valparaíso*, pages 53–58.

Silva, N., Calvete, C., and Sievers, H. (1997). Características oceanográficas físicas y químicas de canales australes chilenos entre Puerto Montt y Laguna San Rafael (Crucero CIMAR-Fiordo 1). *Ciencia y Tecnología del Mar (Chile)*, 20:23–106.

Silva, N., Rojas, N., and Fedele, A. (2009). Water masses in the Humboldt Current System: Properties, distribution, and the nitrate deficit as a chemical water mass tracer for

Equatorial Subsurface Water off Chile. *Deep Sea Research Part II: Topical Studies in Oceanography*, 56(16):1004–1020.

Silva, N., Sievers, H., and Prado, R. (1995). Características oceanográficas y una proposición de circulación, para algunos canales australes de Chile entre 41 20's y 46 40's. *Revista de Biología Marina*, 30(2):207–254.

Skamarock, W. C., Klemp, J. B., Dudhia, J., Gill, D. O., Liu, Z., Berner, J., Wang, W., Powers, G., Duda, M. G., Barker, D. M., and Huang, X.-Y. (2019). A description of the advanced research WRF model version 4. Report, National Center for Atmospheric Research.

Soto-Mardones, L., Letelier, J., Salinas, S., Pinilla, E., and Belmar, J. P. (2009). Análisis de parámetros oceanograficos y atmosfericos del Seno de Reloncaví. *Gayana (Concepción)*, 73:141–155.

Strub, P. T., James, C., Montecino, V., Rutllant, J. A., and Blanco, J. L. (2019). Ocean circulation along the southern Chile transition region (38°–46° s): Mean, seasonal and interannual variability, with a focus on 2014–2016. *Progress in Oceanography*, 172:159–198.

Sutherland, D. A. and Cenedese, C. (2009). Laboratory experiments on the interaction of a buoyant coastal current with a canyon: Application to the East Greenland current. *Journal of Physical Oceanography*, 39(5):1258–1271.

Syvitski, J. P. M., Burrell, D. C., and Skei, J. M. (1987). *Fjords: Processes and Products*. Springer, New York.

Tonini, M. and Palma, E. (2009). Circulación residual y vorticidad mareal en los golfos Norpatagónicos. *Mecánica Computacional*, 28(34):2851–2867.

Tonini, M. H. and Palma, E. D. (2011). Respuesta barotropica de los golfos norpatagonicos argentinos forzados por mareas y vientos. *Latin American Journal of Aquatic Research*, 39(3):481–498.

Vortmeyer-Kley, R., Holtermann, P., Feudel, U., and Gräwe, U. (2019). Comparing eulerian and lagrangian eddy census for a tide-less, semi-enclosed basin, the Baltic Sea. *Ocean Dynamics*, 69(6):701–717.

Vázquez Pinillos, F. J., Chica Ruiz, J. A., and Martínez González, G. O. (2023). La gestión costera en la isla y el mar de Chiloé (Chile): Un diagnóstico de los problemas operativos desde la GIAL y su relación con el cambio climático. *Revista de Geografía Norte Grande*, pages 1–27.

Wang, Y., Hutter, K., and Bäuerle, E. (2001). Barotropic response in a lake to wind-forcing. *Annales Geophysicae*, 19(3):367–388.

Zimmerman, J. T. F. (1981). Dynamics, diffusion and geomorphological significance of tidal residual eddies. *Nature*, 290(5807):549–555.

Zimmerman, J. T. F. (1986). The tidal whirlpool: A review of horizontal dispersion by tidal and residual currents. *Netherlands Journal of Sea Research*, 20(2):133–154.